



HAL
open science

Spatio-temporal variability of the morpho-sedimentary dynamics observed on two gravel beaches in response to hydrodynamic forcing

Antoine Soloy, Imen Turki, Nicolas Lecoq, Carlos Lopez Solano, Benoît B. Laignel

► To cite this version:

Antoine Soloy, Imen Turki, Nicolas Lecoq, Carlos Lopez Solano, Benoît B. Laignel. Spatio-temporal variability of the morpho-sedimentary dynamics observed on two gravel beaches in response to hydrodynamic forcing. *Marine Geology*, 2022, 447, 10.1016/j.margeo.2022.106796 . hal-04420293

HAL Id: hal-04420293

<https://normandie-univ.hal.science/hal-04420293v1>

Submitted on 22 Jul 2024

HAL is a multi-disciplinary open access archive for the deposit and dissemination of scientific research documents, whether they are published or not. The documents may come from teaching and research institutions in France or abroad, or from public or private research centers.

L'archive ouverte pluridisciplinaire **HAL**, est destinée au dépôt et à la diffusion de documents scientifiques de niveau recherche, publiés ou non, émanant des établissements d'enseignement et de recherche français ou étrangers, des laboratoires publics ou privés.



Distributed under a Creative Commons Attribution - NonCommercial 4.0 International License

1 Spatio-temporal variability of the morpho- 2 sedimentary dynamics observed on two 3 gravel beaches in response to 4 hydrodynamic forcing

5 Authors

6 Antoine Soloy^{a*}, Imen Turki^a, Nicolas Lecoq^a, Carlos Lopez Solano^a, Benoit Laignel^a

7 ^a: Normandie Univ, UNIROUEN, UNICAEN, CNRS, M2C, 76000 Rouen, France

8 *Corresponding author

9 Abstract

10 This article aims to investigate the 3D morpho-sedimentary dynamics of two gravel beaches in
11 relation to hydrodynamic forcing, using a multi-sensor approach. Study sites, namely Etretat and
12 Hautot-sur-Mer, are both located in Normandy, France. Thus, they face similar wave conditions of
13 the English channel's eastern side, with megatidal ranges and channelized wave orientations.
14 However, they differ in gravel size (D50 Etretat = 5.2 cm; D50 Hautot-sur-Mer = 7.0 cm), vertical
15 composition (Etretat is a purely gravel beach, Hautot-sur-Mer is a composite one with a low tide
16 terrace) and wave exposure (Etretat is an embayed beach, oriented 47°N, Hautot-sur-Mer is a semi-
17 open beach, oriented 71°N). Used data include shoreline positions, automatically extracted from
18 coastal Video Monitoring Systems (VMS) images between 2018 and 2020, wave data provided by the
19 WaveWatch 3 model, and gravel size maps derived from UAV-imagery at different dates (one in
20 Etretat, three in Hautot-sur-Mer). First, an EOF analysis was performed on the shoreline position data
21 to extract the Principal Components (PC) describing mechanisms of morphological changes in the

22 shoreline shape at different elevations (-2 to +3m in Etretat and +1 to +3m in Hautot-sur-Mer). Four
23 mechanisms spread within five PCs were found in Etretat: cross-shore migration (PC1), rollover (PC2),
24 scale/elevation dependent rotation (PC3 and PC4) and breathing (PC5). Four PCs describing three
25 mechanisms were identified in Hautot-sur-Mer: right-centered beach cell rotation (PC1), left-
26 centered beach cell rotation (PC2), larger scale rotation (PC3) and rollover (PC4). Interpretation of
27 the modes were supported by significant correlations with morphological parameters such as
28 average beach width (BW), beach orientation angle (BOA) and beach slope (BS). The mid-term
29 morphological main periods of variability include 2, 3, 5 and 8+ months in Etretat, and 2, 3 and 6
30 months in Hautot-sur-Mer (all parameters included), which essentially corresponds to the variability
31 of the wave energy. Finally, the analysis of surface grain size spatial variability revealed the presence
32 textural patterns with spatial temporal variations in sorting and average grain size up to 1 cm in two
33 months.

34 Keywords

35 Shoreline variability; pebble beach; cross-shore translation; beach rotation; beach breathing; beach
36 rollover

37 Highlights

- 38 • Gravel beaches experience rotation, migration, breathing & rollover mechanisms
- 39 • Identified mid-term main periods of variability include 2, 3, 5, 6 and 8+ months
- 40 • Changes in BW, BOA and BS are mainly related to wave forcing
- 41 • Grain size sorting and mean size evolutions are likely seasonal

42 1. Introduction

43 Monitoring, understanding, and predicting coastal dynamics are key issues in coastal engineering in
44 order to cope with coastal risks, especially in the context of climate change and sea level rise. It is a
45 challenging task as coastal morphodynamics are the complex result of non-linear interactions
46 between hydrodynamic forcing (currents, waves, tides) and local characteristics (sediment size,
47 embayment, intertidal zone structuration, etc.). Over the past few decades, great progress has been
48 made in this regard thanks to improved monitoring technologies, which now allow the study of

49 coasts at different scales, from the global and regional ones through satellite imagery, to the local
50 scale through ground surveys and video monitoring systems (VMS).

51 Satellite techniques rely on data provided by optical or radar sensors to identify coastal features at a
52 regional or larger scale, at a daily to weekly measuring frequency constrained by orbital parameters
53 (Salameh et al., 2019; Vos et al., 2020). “Ground surveys” gathers all the methods for in situ
54 measurement of a site’s topography of at a defined moment, including lidar, total stations,
55 differential GNSS (dGNSS) and photogrammetry (Andriolo et al., 2018; Lee et al., 2013; Mason et al.,
56 2000; Morton et al., 1993). Among them, the profiling methods (dGNSS and total stations) are
57 particularly used for long term repeated measurements as the method is relatively versatile and can
58 provide morphological monitoring records down to the hourly scale. Nevertheless, measurements
59 are most often carried on at a weekly to monthly frequency and sometimes even shorter, depending
60 on research specific needs (Lacey and Peck, 1998; Larson and Kraus, 1994; Turner et al., 2016).

61 The use of VMS is a popular methodology that made it possible to monitor the shoreline of specific
62 study sites on the long term, at daylight, with high resolution (from centimeters to meters), applying
63 a commonly used sampling time step of 10 minutes (Davidson et al., 2007; Holman and Stanley,
64 2007; Silva et al., 2009; Turner et al., 2004). The idea is to georeference the moving shoreline visible
65 on images, using its pixel coordinates associated with the local water level, assuming a good
66 knowledge of the cameras' position and orientation relative to the environment in their field of view
67 (Aarninkhof et al., 2003). Using this technique makes it possible to monitor the intertidal morphology
68 with a repeatability up to the tidal cycle, although consistently delineating the shoreline over long
69 periods can be challenging due to the high variability of image-taking conditions (light, weather, sea
70 states, boats, users, camera lens cleanness, etc.). Authors report vertical biases ranging from 10 to
71 34 cm on reconstructed intertidal digital elevation models, depending on the site, hardware, dataset
72 and delineation method used (Plant et al., 2007; Soloy et al., 2021; Uunk et al., 2010).

73 VMS data are often processed with an Empirical Orthogonal Function (EOF) statistical analysis in
74 order to decompose the complex movements of the shoreline through time into simpler components
75 of variability, each of which summarizes a certain part of the total variability. By doing this, authors
76 were able to identify mechanisms such as cross-shore migration, beach rotation (Blossier et al., 2017;
77 Harley et al., 2015; Robinet et al., 2020; Turki et al., 2013), breathing (Blossier et al., 2017; Ratliff and

78 Murray, 2014; Robinet et al., 2020), boundary effect of cross-shore structures (Miller and Dean,
79 2007), nourishment effects (Lemke and Miller, 2017), and even geological variations (Hapke et al.,
80 2016). However, this improvement in monitoring techniques has mostly benefited the understanding
81 of sandy coastal systems, and our knowledge of gravel ones remains relatively modest in
82 comparison, despite the fact that they represent a significant - although unknown - part of the
83 world's coastline (Buscombe and Masselink, 2006; Jennings and Shulmeister, 2002; Mason and
84 Coates, 2001; Van Wellen et al., 2000). The main reason for this discrepancy is probably the cost and
85 difficulty of measuring the spatial variability of gravel particle size, as well as its temporal variability,
86 although this information is thought to be essential to understand and model the dynamics of gravel
87 beaches (Buscombe and Masselink, 2006). Indeed, the spatial variability of gravel sizes and shapes as
88 well as their temporal variabilities play a significant role in the reciprocal relationship between
89 sediment transport, hydrodynamic processes, and morphological changes (Bluck, 1967; Buscombe
90 and Masselink, 2006; Flemming, 1964; Isla, 1993; Orford, 1975; Williams and Caldwell, 1988).

91 To address this disparity and take the variability of sediment characteristics into account, the present
92 study aims to investigate the geomorphodynamics and gravel size variability of two coastal systems,
93 Etretat and Hautot-sur-Mer, a purely gravel beach and a composite one, respectively, both located in
94 Normandy, France (Figure 1). Using the methodology developed by Soloy et al. (2021) and applied to
95 nearly two years of VMS image data, it was possible to automatically monitor the shoreline position
96 on both beaches on various elevations within the tidal range. Combined with the other recently
97 developed algorithm from Soloy et al. (2020), with the aim of mapping the distribution of surface
98 gravel particle size at different times, this paper intends to propose a first analysis of the morpho-
99 sedimentary relationship of two pebble beaches of Normandy.

100 The extracted information will help us answer different questions regarding morphodynamics and
101 sedimentary variability of gravel beaches in Normandy, including: (1) How does the shoreline shape
102 changes through time? (2) Are changes homogeneous at all elevations? (3) Are there specific
103 mechanisms of shoreline change and what are their typical temporal period of variability? (4) What
104 physical phenomena are responsible for morphological changes? (5) What is the shoreline's fabric
105 made of? (6) How do the fabric's properties vary through time? (7) Can we link the morphological
106 variability to the sedimentary one?

107 To bring relevant solutions to this questioning, an Empirical Orthogonal Function (EOF) analysis was
108 performed using VMS-derived intertidal bathymetry datasets in order to identify the different
109 mechanisms describing the shoreline variability at various elevations. Then, a wavelet analysis was
110 used to identify and compare the main periods of variability of morphological parameters (beach
111 width, beach orientation angle and beach slope) with hydrodynamic ones (wave energy, current
112 speed, and tidal range), and determine the main acting physical forcing processes. Finally, the spatial
113 and temporal variability of gravel size were analyzed in light of the results brought by previous
114 analysis.

115 This study is articulated around 5 sections, the first of which is this introduction. Section 2 presents
116 the study sites and is succeeded by a material and methods description in section 3. Results are
117 presented and discussed in section 4, and conclusive remarks are provided in the fifth and final
118 section.

119 2. Study sites

120 The present study focuses on the shoreline dynamics of the pebble beaches of Hautot-sur-Mer and
121 Etretat. These two sites are located along the coast of Normandy, France, on the Southeast side of
122 the English Channel (Figure 1). The funnel morphology of the Channel produces extreme tidal ranges
123 called megatidal (up to 15 m at Mont Saint Michel, Bonnefille (1968); Chabert D'Hières and Le
124 Provost (1978); Levoy et al. (2000); SHOM (1953)) and orient the wave propagation in the channel
125 extension's direction (SW - NE).

126 Hautot-sur-Mer is a composite beach (Jennings and Shulmeister, 2002) with a steep slope (>10%)
127 pebble ridge (measured D50 = 7.1 cm) laying on sandy low tide terrace (measured D50 = 0.18 mm)
128 (Figure 2). It is a 1100 m long semi-open beach with a linear plan-form shape, installed in the hollow
129 of a valley and surrounded by chalk cliffs. The beach has nine groins installed perpendicularly to a
130 seawall oriented at 71°N. The tidal range measured at Dieppe (4.5 km East of the study site) varies
131 from 2.96 m in neap to 9.86 m in spring tide, with an average amplitude of 6.79 m (Table 1). The
132 gentle slope of the sandy low tide terrace (1.3%) allows the water to retreat over 210 m away from
133 the seawall at the lowest tides. The average wave height is 0.79 m heading 130°N, with a yearly
134 maximum of 3.55 m for the year 2019.

135 Etretat is a 1000 m long embayed purely gravel beach with a parabolic plan-form shape, installed at
136 the outlet of a valley and surrounded by chalk cliffs. The beach is composed of a steep slope (>12 %)
137 pebble ridge (measured D50 = 5.2 cm) (Figure 2). A subtidal sandy substrate (measured D50 = 0.8
138 mm) (Soloy et al., 2020) appears on rare occasions when the beach becomes mainly sandy after long
139 repetitive heavy storm conditions. The beach is crossed by 4 groins installed against the seawall,
140 which has a mean orientation of 47°N. In the intertidal zone, bedrock emerges at low tide on the
141 sides of the bay. The tidal range varies from 3.2 m to 9.13 m, with an average of 6.08 m. At low tide,
142 the beach width can reach 150 m (Table 1). The average wave height is 0.89 m heading 145°N, with a
143 yearly maximum of 4.44 m for the year 2019.

144 3. Material and methods

145 3.1. Nearshore Hydrodynamics

146 The hydrodynamic parameters of this study were used to serve two different purposes: (1)
147 estimating the beaches' 3D morphology using VMS-derived waterlines of known elevation (water
148 level), and (2) comparing morphodynamics with hydrodynamics (wave energy, tidal currents, tidal
149 ranges).

150 For measuring the morphology (georeferencing the waterlines) in Hautot-sur-Mer, water level data
151 was provided by the tide gauge ran by the French Naval Hydrographic and Oceanographic Service
152 (Service Hydrographique et Oceanographique de la Marine, SHOM) and located in the harbor of
153 Dieppe (49° 55' 45.0114"N, 1° 5' 4.1634"E), 4.2 km North East from the VMS ([https://doi.org/
154 10.17183/REFMAR#24](https://doi.org/10.17183/REFMAR#24)). Unfortunately, there exist no other hydrodynamics observation station near
155 the study sites. Hence, other hydrodynamic parameters were extracted from hindcast model
156 outputs.

157 As there is no tidal gauge anywhere near Etretat, water levels (tide and surge) used for estimating
158 the morphology of the beach were provided by the Hycom2D model (Chassignet et al., 2007). The
159 model's output is given on a curvilinear grid with a resolution ranging from 2 km far from the coast to
160 500 m close to the coasts. The time series was extracted from the point of coordinates
161 49° 42' 45.7194"N, 0° 11' 34.4394"E. The maximum error on the water elevation is expected to
162 happen during high surge with an underestimation of 10 cm, while the tidal phase difference

163 uncertainty is 12 min (Pasquet et al., 2014). A comparison between Hycom2D and the water level
164 gauge in Dieppe shows an RMSE of 0.26 m and an R^2 of 0.98 (0.13 m and 0.53 for surge alone). Figure
165 3a presents the time series of water elevations in Etretat used in this study. Elevations are centered
166 around zero and vary from ± 2 m to ± 5 m during the tidal cycle, with a maximum amplitude of
167 9.13 m. It is worth mentioning that setup elevations are not considered by Hycom2D. Consequently,
168 morphological data are projected with a bias that tends to reduce their elevation by an order of
169 magnitude of a few centimeters.

170 Wave data were provided by the implementation of the WaveWatch 3 model (Tolman, 2009) by
171 Ifremer (French Research Institute for Exploitation of the Sea) over the English channel called
172 PREVIMER_WW3-NORGAS-UG (Dumas et al., 2014). The output is given on an unstructured grid with
173 a resolution varying from 2 minutes of arc off the shore to 200 m near the coast. Data were extracted
174 at the point $49^\circ 42' 53.7114''\text{N}$, $0^\circ 10' 58.35''\text{E}$ for Etretat (depth $h = 21$ m), and at the point
175 $49^\circ 56' 55.5936''\text{N}$, $1^\circ 1' 2.7042''$ for Hautot-sur-Mer (depth $h = 17.5$ m). This model has been
176 extensively validated with data from buoys and satellite altimeters (Michaud et al., 2015) showing
177 Root Mean Square Errors (RMSE) of 25 cm and coefficients of determination (R^2) of 0.94 on the sea
178 surface wave significant height parameter (H_s) (Castelle et al., 2020). Output parameters used in this
179 study include H_s and wave direction, from July 2018 to November 2020.

180 Figures 3b and c present the wave significant height and period respectively in Etretat, as used in the
181 present study. During the period 2018 – 2020, the average H_s was 0.88 m with a maximum of 4.44 m,
182 and the average peak period was 7.0 s with a maximum of 18.2 s. Both parameters show a
183 seasonality with higher values during winter (October to April) and lower values during summer
184 (April to October). Energetic events take place mainly during winter seasons like the storm Ciara
185 recorded on 10th of February 2020 when waves reached 4.44 m in height.

186 Wave roses presented in Figures 3e and f show that there are two main incoming wave directions:
187 West and North. During winter, 71.6 % of waves are coming from the Western sector ($250^\circ\text{N} -$
188 310°N), and especially 50.0 % come from directions ranging between 270°N and 290°N , with a
189 maximum height of 4.44 m. The Northern sector ($0^\circ\text{N} - 30^\circ\text{N}$) hosts 14.0 % of the waves with a
190 maximum wave height of 2.76 m. On the other hand, summer waves are coming from the Western
191 sector 59.6 % of the time, 49.3% of the waves being concentrated between directions 270°N to

192 290°N, with a maximum wave height of 3.30 m. The Northern sector hosts 26.1 % of the waves with a
193 maximum height of 3.16 m.

194 For each site, wave characteristics were used to calculate the energy flux EF .

$$195 \quad EF = E \times C_g$$

196 Where EF is the total wave energy determined using $E = \frac{1}{8} \times \rho \times g \times H_S^2$, and C_g is the wave group
197 velocity given by $C_g = \frac{c}{2} \left(1 + \frac{2kh}{\sin(2kh)} \right)$, h is the water depth, k is the wave number $k = \frac{2\pi}{L}$, L is the
198 wavelength, and c is the wave celerity in transitional water $c = \frac{gT}{2\pi} \tanh(kh)$, g is the acceleration of
199 gravity of 9.81 m/s, and T is the wave period.

200 This allows us to project EF along the cross-shore and longshore local axis of the beach:

$$201 \quad EF_C = EF \times \cos(\alpha)$$

$$202 \quad EF_L = EF \times \sin(\alpha)$$

203 Where EF_C and EF_L represent the cross-shore and the longshore projections respectively, and α is
204 the angle between the incoming waves and the beach orientation.

205 3.2. Shoreline Variability

206 Video Monitoring Systems (VMS) were installed in June and December of 2018 respectively in Etretat
207 and Hautot-sur-Mer. The VMS implementation and operational processing are presented and
208 discussed in detail in a dedicated article (Soloy et al., 2021). For each site, 3 video cameras cover a
209 panoramic view of the beaches (Figure 4), recording time-averaged images (timex) every 10 minutes
210 and over 10 minutes during daylight. A Mask R-CNN segmentation model (He et al., 2017) is used to
211 automatically delineate the waterline on images. Produced lines are then georeferenced and
212 clustered per tidal cycle in order to generate daily intertidal point-clouds. RMSE values show a
213 vertical elevation mean uncertainty of 22 cm in Etretat and 29 cm in Hautot-sur-Mer, which are
214 within the range of values calculated by authors for other sites (Plant et al., 2007; Uunk et al., 2010).

215 On both sites, the morphological variability of the beach was evaluated through the analysis of three
216 morphological indices: the beach width (BW), the beach slope (BS) and the beach orientation angle
217 (BOA). These indices were extracted from our VMS-derived point clouds datasets.

218 BW is obtained by measuring the cross-shore distance separating waterlines to a predefined baseline
219 along cross-shore transects (Figure 5). In total, the beaches are segmented into 211 and 114
220 transects for Etretat and Hautot-sur-Mer, respectively. Each transect starts from a perpendicular
221 baseline located along the beach's seawall where it is separated by 2 m from its neighbors. Transects
222 are all 100 m long while heading towards the sea and do not cross each other. BW is the horizontal
223 distance separating the baseline to a point of fixed elevation along each transect. Target elevations
224 range from -2 m to +3 m in Etretat (0 m being the local mean water level), and from +1 m to +3 m in
225 Hautot-sur-Mer, and are vertically separated by 1 m. When no waterline was recorded at the exact
226 target elevation, an interpolated value between the neighbor waterlines was used. Elevation limits
227 indicated below were constrained by data availability throughout the tidal cycle. The lower number
228 of elevations in Hautot-sur-Mer is due to the difficulty of identifying a clearly contrasted shoreline on
229 the lower part of the composite system ($z < +1$ m).

230 BS was computed as the slope $\frac{\Delta z}{\Delta x}$ along each transect, and between neighboring target elevation.

231 BOA is calculated by approximating the shoreline to a parabola. The orientation angle is then
232 calculated as the angle between the seawall and the parabola's tangent of a selected transect. On
233 both sites, the transects located at the center between two groins were chosen to compute the BOA:
234 P050 in Etretat and P075 in Hautot-sur-Mer.

235 For all parameters, values were averaged at a daily time scale, and gaps were filled with linearly
236 interpolated ones. On both sites a malfunction disabled the right-side camera in November 2019 in
237 Etretat and in June 2020 in Hautot-sur-Mer. Consequently, the lateral extension of the beach being
238 monitored changed through time. Thus, our analysis will focus only on the profiles that remained in
239 the left and center camera frames in Etretat, i.e., transects from P20 to P114 (from July 2018 to June
240 2020), and only take into account the dates at which the right camera was still working in Hautot-sur-
241 Mer, i.e., from December 2018 to June 2020 (with transects from P20 to P99), in order to maximize
242 both the duration and beach lateral extension being analyzed.

243 This approach allows the study of one beach cell bounded with two groins on the sides and the sea
244 wall at the back for the two sites, which is here considered a local morphological unit whose
245 evolution remains a good approximate to the one of the larger scale coastal system. In Hautot-sur-

246 Mer, the available data covers the halves of two different boxes siding the groin located at P50
247 instead of a full one. Assuming that morphodynamics can be considered consistent from one box to
248 its direct neighbors as long as they remain similar in size, shape, composition and orientation, it is
249 assumed that results are representative of a full unit. The studied beach cell length is 188 m long in
250 Etretat and are 100 and 140 m long in Hautot-sur-Mer for both the West and the East cells,
251 respectively.

252 3.3. Grain Size Mapping

253 The spatial variability of the sediment size was measured using the methodology developed by Soloy
254 et al. (2020). This method relies on the use of the Mask R-CNN algorithm to automatically detect and
255 classify the non-overlapping clasts visible on an image at the pixel scale. The size of the detected
256 clasts can then be measured along the long and short axis of the ellipse that fits the best to their
257 contour. Using georeferenced ortho-imagery, it is possible to map the spatial spread of sediment size
258 over large areas (typically a few tens of thousands of square meters), at the scale of single clasts.
259 Measurements provided by this method were validated with $R^2 = 0.98$ and $RMSE = 3.9$ mm using
260 pebbles from Hautot-sur-Mer.

261 Ortho-images were produced using Structure from Motion (SfM) techniques applied on UAV data
262 (Westoby et al., 2012). The UAV measurement campaigns took place on 2020/06/10 in Etretat, and
263 on 2019/04/09, 2019/06/04 and 2020/06/09 in Hautot-sur-Mer. The maps used for this study were
264 produced by averaging the sediment long axis size using a grid of resolution 1 m x 1 m.

265 3.4. Statistical approaches

266 The analysis of the evolution of the beaches' morphology was performed using Empirical Orthogonal
267 Functions (EOF). This statistical method was proven relevant to extract spatio-temporal variability
268 patterns in time series of shoreline position (Aubrey, 1979; Medina et al., 1994, 1993; Turki et al.,
269 2013; Winant et al., 1975).

270 The objective of this approach is to extract variability modes along both spatial and temporal
271 dimensions, and to quantify their dependance from the original time series of 2D shoreline positions
272 $Y(t, x)$. To do so, a map of linear regressions and correlations is calculated, the axis of maximum
273 amplitudes determines the first spatial and temporal eigenfunctions, $E_1(x)$ and $C_1(t)$, respectively.

274 The first functions' variability is then subtracted from the time series, and the same procedure is
275 applied again to define the second eigenfunctions along an orthogonal axis. The methodology is
276 iteratively repeated from $k = 1$ to $k = n$, where n is reached when the cumulative variance
277 explained by all eigenfunctions reaches a previously defined threshold. Therefore $Y(t, x)$ can be
278 described as a series of linear combinations of both spatial and temporal eigenfunctions.

$$279 \quad Y(t, x) = \sum_{k=1}^n C_k(t) \cdot E_k(x)$$

280
281 Along with the EOF, the correlation factor r was often used in this paper to evaluate the linear links
282 between different parameters.

$$283 \quad r = \frac{Cov(X, Y)}{\sigma_X \times \sigma_Y}$$

284 Where $Cov(X, Y)$ is the covariance between two vectors X and Y , as calculated by $Cov(X, Y) =$
285 $E[(X - \bar{X}) \times (Y - \bar{Y})]$.

286 r values can range from -1 to 1. However, as there was no need to discriminate negative from
287 positive correlations along this study, r here refers as the absolute correlation value, therefore
288 varying from 0 to 1. Correlation values r superior to 0.5 were considered significant.

289 The temporal evolution of signals was also investigated using a wavelet analysis. The wavelet
290 transform is a high-resolution frequency analysis technique that consists of decomposing a signal in
291 both time and frequency in order to describe both periodic and non-periodic changes.

292 A wavelet transform is used to decompose the signal based on children wavelet, which correspond to
293 scaled and translated versions of a reference parent wavelet. Each wavelet has a finite length (a
294 scale) and is localized in time. The parent wavelet includes two parameters for time-frequency
295 exploration: a scale parameter a and a temporal localization parameter b .

$$296 \quad \Psi_{a,b}(t) = \frac{1}{\sqrt{a}} \Psi_0\left(\frac{t-b}{a}\right)$$

297 The parameterization in scales and the translation of the children wavelet allows the detection of the
298 different frequencies composing the signal. The continuous wavelet transform of a signal $S(t)$

299 produces a local wavelet spectrum, as defined by $C(a, b) = \int_{-\infty}^{+\infty} x(t) \cdot \Psi_{a,b}(t) \cdot dt$. The local wavelet
300 spectrum allows a description and visualization of the power distribution (color axis) along the
301 different frequencies/periods (y axis) over time (x axis).

302 The wavelet power can then be averaged at each period to obtain the global wavelet spectrum
303 (GWS), which highlights the periods (modes) of variability present in the signal.

304 4. Results and discussions

305 4.1. Morphological changes in shoreline position

306 The spatial and temporal variability of the shoreline position of Etretat and Hautot-sur-Mer beaches
307 was investigated using 2 years of daily observations. The shoreline position at elevations ranging -2 m
308 to +3 m (1 m step) from mid-2018 to late 2020 in Etretat, and at elevations +1 m to +3 m from early
309 2019 to mid-2020 in Hautot-sur-Mer, are presented in Figure 6a and 6b, respectively. Time series of
310 the average BW at each elevation are shown in Figure 6c and 6d, as well as the average planform
311 shape of the shoreline in Figure 6e and 6f.

312 As a first observation, the shorelines' planform shapes visible on Figure 6a, b, e, and f differ from one
313 site to the other. In Etretat, the shoreline adopts the shape of a parabola with a center part being
314 closer to the seawall than both of its ends near Groins 1 and 2. The shape is more linear in Hautot-
315 sur-Mer where the right side of a cell (left side of groins) is on average farther from the seawall than
316 the left one (right side of groins). Regarding cross-shore slopes, Figure 6e shows the increasing slope
317 with height, from around 0.14 between -2 m and -1 m, to 0.25 between +2 and +3 m. The small
318 bump visible at each elevation on a diagonal from P70 at -2 m to P80 at +3 m corresponds to a small
319 discrepancy in camera alignments that is also visible on Figure 6a. In Hautot-sur-Mer (Figure 6f), the
320 average slope is 0.10 between +1 m and +2 m, and 0.12 between +2 m and +3 m. Although the
321 smaller number of elevations does not allow for the lower profile to be evaluated here, a slope of
322 0.013 was measured on the sandy substrate by Soloy et al. (2020).

323 On Figure 6a and 6b, the succession of reddish and blueish colors corresponds to a series of advance
324 and retreat movements. Changes are differently manifested along the beach, especially in Hautot-
325 sur-Mer where the wide side changes from west to east through time. This variation is likely
326 associated with a beach planform rotation around a pivotal point generated by the wave diffraction

327 near the groins and its obliquity responsible for a longshore transport. Figure 6b suggests a
328 seasonality in the rotation mechanism with an alternance between two main beach orientations: (1)
329 a wider side to the left of the beach cell (beach facing NE) from April to August, and (2) a wider side
330 to the right (beach facing NW) throughout the rest of the year.

331 In Etretat, the time series of average BW Figure 6c do not show any clear seasonal pattern. The +3 m
332 beach width consistently retreats from 30 m in July 2018 to 20 m in December 2019. It then suddenly
333 reaches its low around 12 m where it remains from December to April 2020 before advancing to 30
334 m again by April – May, where it remained until the end of the series. The period of retreated
335 shoreline observed from December to April 2020 corresponds to a series of severe winter storms.
336 During this series of storms, an old groin that is usually covered by sediment emerged around P60 in
337 Etretat, thanks to erosion, and the top of the beach even became sandy for a few weeks. At the
338 bottom of the beach, the -2 m beach width consistently remained around 60 m, with no significant
339 change during winter 2020, but advancing towards 63 m on average at the end of the storm period.

340 In Hautot-sur-Mer, a subtle seasonality pattern is visible in the time series of beach width with values
341 evolving from 25 m in December to 30 m in July, at +3 m of elevation and from 33 to 38 m at 0 m at
342 the same dates. The amplitude of daily changes also evolves with 2 to 3 m on average during summer
343 seasons up to 7 to 8 m during winter ones. However, the early 2020 series of storm events did not
344 provoke a period of minimum beach width similar to the one in Etretat, although large variations are
345 visible during this period.

346 Despite their proximity, both sites present significant morphodynamical differences. The difference
347 in shoreline planform shapes is first explained by the difference in openness between both
348 coastlines: embayed/enclosed beaches like Etretat naturally adopt a concave shape while open
349 beaches are more linear at a large scale. At the scale of the beach cell, groin structures also play a
350 role in the shoreline shape by accumulating the alongshore-drifted sediment on one side while
351 creating a deficit on the other side. The effect of groins on the shoreline planform shape was
352 modeled by Leont'yev (2018, 2007), who showed that the planform shape consecutive to the
353 presence of groins can be summarized as a linear function for the accumulative side of the groin, and
354 as a sinusoid for the erosive one. The extent of the groin's influence zone depends on both groin
355 characteristics (size, elevation, spacing, etc.) and the alongshore sediment flux characteristics

356 (discharge, channel size, etc). If the inter-groin distance is lower than the one-sided extent of their
357 influence given a certain sediment flux, the erosive side of a groin will interact with the accumulative
358 side of its neighbor. This interaction limits the development of a sinusoid pattern, resulting on a more
359 linear shoreline such as what can be observed in Hautot-sur-Mer. The average left facing planform
360 shoreline orientation also suggest an asymmetric longshore drift in a West to East direction, which is
361 confirmed by the observations of Costa et al. (2015). The location of Etretat near the Cape of Antifer
362 where the sediment alongshore drift asymmetry lower (Costa et al., 2015) allows the average inter-
363 groin planform shoreline to be more parabolic, thanks to the more even permutations between
364 accumulative and erosive sides of groins (Leont'yev, 2018).

365 Etretat seems to be more sensitive to the impact of storms than Hautot-sur-Mer, and especially
366 clustered ones. The influence of storm clustering on the eroded sediment volume was shown by
367 Karunarithna et al. (2014) to be largely higher on than the one of individual storms on sandy
368 beaches. Assuming that the same phenomenon happens with coarser sediment, it could explain the
369 observed retreat in Etretat. The reason why Hautot-sur-Mer does not experience the same retreat is
370 probably due to the protection offered by the dissipative low tide terrace. Indeed, Almeida et al.
371 (2014) were able to compare the offshore significant wave height to the onshore one on different
372 types of beaches and showed that storm wave height was reduced by a factor of 2 to 2.5 on
373 composite beaches due to the low tide terrace dissipative effect, while wave height was not reduced
374 and even be slightly increased on purely gravel beaches.

375 The transition from gravel to sand by erosion in Etretat during the storm period changed the
376 properties of the fabric exposed to the waves, likely lowering its permeability (Krumbein and Monk,
377 1943) while still offering a reflective profile to incoming waves, although more gently sloped. Hay et
378 al. (2014) reported similar observations on a mixed sand gravel beach of Canada, with a decrease in
379 surficial sediment median diameter when the wave energy was increasing. The consecutive relative
380 stability of the +2 m and +3 m beach width at this period while lower elevations present a higher
381 variability is a phenomenon observed by Karunarithna et al. (2012), who explained that composite
382 beaches may become unstable during storms due to the cutback of the upper beach during a
383 previous storm. Although Etretat's beach is considered purely gravel, this transition from gravel to
384 sand makes it somewhat comparable to a composite one. Our hypothesis is that the gravel sediment

385 eroded from the top of the beach was deposited at the subtidal bottom, unmonitored, thus building
386 the beach step and providing a focus point to stabilize the runup extent and the swash to lower
387 elevations, thus protecting the upper beach, as already evidenced on a gravel beach by Poate et al.
388 (2013).

389 4.2. Principal Components of Variability

390 EOF were calculated using time series of average beach width at the various selected elevations with
391 the aim of extracting principal components (PC) of morphological variability to characterize the
392 beaches' spatiotemporal morphodynamics. Each PC describes a percentage of the shoreline's total
393 variability through space and time between -2 m and +3 m in Etretat (Figure 7), and from +1 m to +3
394 m in Hautot-sur-Mer (Figure 8). Linear correlation coefficients were then calculated between
395 different components and morphological parameters (BW, BS, BOA and PCs), and with
396 hydrodynamical ones (wave energy, current speed, and tidal range). The result correlation matrices
397 are presented in Figure 9. In all cases, the significance threshold is set to 0.5 which is the
398 conventional value for rejection of the null hypothesis (absence of correlation). Figure 10 presents a
399 conceptual model describing how and to which spatial extent is each PC related to one or several
400 mechanisms.

401 Table 2 presents the percentage of the total variability explained by each PC. Results show that up to
402 six PCs are necessary to explain at least 90% of the total variability of Etretat's shoreline position. In
403 Hautot-Mer, the number of PCs required to reach the same threshold is 14, thus showing higher
404 complexity. Therefore, the threshold of cumulated explained variability was lowered to 80% for this
405 site, although it still includes up to 7 PCs. However, PC6 in Etretat and PC5 to 7 in Hautot-sur-Mer are
406 considered residual in further discussion as their behavior is erratic and their relative variability
407 remains low. For both sites, the first PC explains around half of the total variability, with 62.4% in
408 Etretat and 46.1% in Hautot-sur-Mer. Further PCs account for significantly lower amounts, although
409 similar from site to site.

410 Figure 7 presents the results of the EOF in Etretat. Both spatial ($E_k(x) \times E_k(y)$) and temporal ($C_k(t)$)
411 eigenfunctions are presented at the top and at the bottom of each PC's subfigure, respectively.
412 Elevations are displayed on an inversed axis to make the figure's top correspond to the sea side,
413 while the bottom is the land side. Dashed black lines locate the position of groin structures, and the

414 black line represents the stability line (i.e., line of zero variability). The red line on figures of $C_k(t)$ is
415 the equivalent stability through time.

416 4.2.1. Etretat

417 *PC 1 – Cross-shore migration*

418 On Figure 7a, $E_1(x) \times E_1(y)$ shows consistent positive values with no crossing of the stability line,
419 which indicates that the entire region moves all together in the same direction, either seaward or
420 landward. The magnitude of variability is larger towards the high elevation left side than the low
421 right side. Therefore, PC1 depicts a cross-shore migration mechanism, with an alternation between
422 advances and retreats. McCarroll et al. (2019) observed that cross-shore mechanisms tend to
423 become significant on embayed beaches longer than 1 km, which agrees with our observation.
424 However, the subtle longshore gradient indicating slightly larger magnitudes on the left side than the
425 right one suggests that the observed migration could be related to a rotation mechanism at the
426 scale of the entire beach. A small drop is visible around the buried groin at the highest elevations,
427 which tends to show the structure's ability to lower the cross-shore variability.

428 Although $C_1(t)$ does not show a specific seasonal variability, it resembles the time series of BW
429 (Figure 6c), including a period of significantly lower values between December 2019 and April 2020,
430 which corresponds to the storm period mentioned in section 4.1. Positive values correspond to
431 advanced shoreline positions while negative ones reflect a retreated state.

432 PC1 is primarily correlated to BW with values ranging from 0.72 to 0.96 (Figure 7a), and to a lower
433 extent is also correlated to BOA with values from 0.52 to 0.56 (except for elevation -2 m with $r = 0.38$
434 and 0.36, respectively). The link observed between PC1 and BOA remains difficult to explain with our
435 data alone, although it could be the manifestation of an alongshore gradient in the cross-shore wave
436 energy such as the one observed by Harley et al. (2015).

437 Regarding hydrodynamics (Figure 7c), none of Etretat's PCs is significantly correlated to any of the
438 considered parameters at the 0.5 threshold. It is generally accepted that hydrodynamics alone are
439 not enough information to the shoreline position change of gravel systems, and that the spatial
440 dispersion of gravel sizes and shapes and their temporal variability are necessary to be considered

441 (Buscombe and Masselink, 2006), therefore low correlation values between hydro- and
442 morphodynamical parameters is not surprising.

443 *PC 2 – Rollover*

444 Figure 7b presents PC2, which describes an alternation between states of advanced shorelines at low
445 elevations while high elevations shorelines are retreated, and the opposite. This would correspond to
446 a mechanism of beach rollover (Buscombe and Masselink, 2006) affecting the beach slope, whose
447 axis of rotation would be located around elevations 0 m and +1 m, according to the alongshore-
448 extended stability line's location on the $E_2(x) \times E_2(y)$ subfigure. To the authors' knowledge, it is the
449 first time that a rollover mechanism is identified using an EOF analysis applied on a shoreline position
450 dataset, although this process is important especially for gravel beaches (Austin and Masselink, 2006;
451 Buscombe and Masselink, 2006), and was often described in the literature (e.g. Isla and Bujalesky
452 (2000); Odezulu et al. (2018); Talavera et al. (2018)).

453 $C_2(t)$ shows a negative trend that could be interpreted as a decreasing tendency of the beach slope
454 throughout the two years of monitoring. Positive values translate a steep slope and negative values
455 correspond to a gentle slope. Buscombe and Masselink (2006) described the rollover process as a
456 response to storms, which seems to be the case on $C_2(t)$, for instance with the storm of January
457 2020 that significantly lowered the slope. But $C_2(t)$ variability appears to be more complex,
458 especially considering the negative trend, and it is likely that other factors might be responsible for a
459 significant part of it such as climate parameters (e.g. Sea Level Pressure, see Montaña et al., 2020),
460 intrinsic characteristics (e.g. granulometry, permeability, etc.), or larger scale mechanisms (e.g. global
461 rotation).

462 Regarding correlations to morphological parameters, PC2 is expectedly well correlated to BS ($r =$
463 0.82). However, it also shows significant correlations with BW at -1 m and -2 m ($r = 0.6$ and 0.83,
464 respectively), while these elevations were the ones presenting the lowest correlations between BW
465 and PC1. This observation shows that the lower the elevation, the lesser the response of the
466 shoreline to cross-shore migration processes, and the larger its link with rollover processes.

467 *PC 3 – Breathing*

468 Figure 7c presents PC3, a breathing mechanism, first described by Ratliff and Murray (2014), and
469 defined as “changes in shoreline curvature as [sediment] move from the middle of the [beach cell] to

470 the edges, and back". Indeed, $E_3(x) \times E_3(y)$ draws two stability lines developed in the alongshore
471 direction and separating the site into 3 alongshore extended regions: high ($z > +1$ m), intermediate (-
472 $1 < z < +1$ m), and low elevations ($z < -1$ m). When both high and low elevations' shorelines are
473 retreated, intermediate ones are advanced, and vice versa. The "eye" shape of this pattern tends to
474 show that the lowest stability line could be extended further to the left towards elevations lower
475 than -2 m, although not monitored here.

476 Interestingly, PC3 shows a cross-shore curvature simultaneous to the alongshore one, but with an
477 even higher magnitude of variability. To the authors' knowledge, this type of cross-shore component
478 in a breathing mechanism was not yet described in the literature. This shows that sediment mostly
479 moves along the cross-shore direction, from low and high elevations towards intermediate ones (i.e.,
480 around the mean sea level) and back.

481 Regarding $C_3(t)$, positive values of correspond to a "deflated" state (i.e., concave cross-shore
482 profile), negative values represent an "inflated" state. The time series presents a seasonal dynamic
483 with on average deflated states during winter and inflated ones during summer. The daily variability
484 is also higher during the winter season. Similar variability was observed in breathing mechanisms by
485 Ratliff and Murray (2014) and Robinet et al. (2020) on embayed beaches, and by Blossier et al. (2017)
486 on a barline. Concerning correlations, $C_3(t)$ presents no significant correlation with any of the tested
487 parameters.

488 *PC 4 – Large scale rotation*

489 PC4 shown in figure 7d is the first mainly longshore mechanism. It is evidenced by the presence of a
490 cross-shore oriented stability line separating two compartments on $E_4(x) \times E_4(y)$, the left one of
491 which is retreated when the right one is advanced, and vice versa. This can be understood as a
492 mechanism of rotation, which generally takes place around a pivotal point and defines retreat
493 movements at one end and advance ones at the other end. The pivotal point was defined by Short et
494 al. (2000) as the point of minimal variability along the beach which here corresponds to the stability
495 line. On present results, the stability line is formed by the succession of pivotal points forms at
496 different elevations.

497 The stability line starts from P90 at the top of the beach (+3 m) and goes towards the left to P50 at 0
498 m, and then goes back towards the right to P80 at -2 m, although one would expect it to be vertical.

499 The change in direction of the stability line at elevation 0 m highlights the existence of a symmetrical
500 process centered on 0 m, with a wider variability at the lowest elevations. These observations
501 indicate that this specific rotation mechanism is likely related to the effect of tides. Indeed, Masselink
502 and Short (1993) showed that tides shift horizontally and vertically the position where processes
503 such as shoaling, surf and swash happen and dissipate the wave energy. Moreover, authors explain
504 that the relative amount of time that the profile is impacted by each process also depends on the
505 tidal range and phasis: Swash has two maximums at both turns of tides. Hence the lowest and
506 highest regions being more variable than the center one. In addition, the oblique stability line could
507 be the result of a change in relative the relative influence of the longshore projection of the swash,
508 due to the same effect. The position of groins does not seem related to any pattern on $E_4(x) \times$
509 $E_4(y)$, the rotation mechanism described by PC4 thus probably describes a mechanism of larger
510 spatial scale than one of the beach cell.

511 Regarding $C_4(t)$, positive values along $C_4(t)$ correspond to a clockwise orientation, negative ones
512 reflect a counterclockwise orientation. The variability is higher during the winter season although
513 there is no clear seasonal pattern: the beach was on average oriented towards opposite directions
514 between January and July of 2019 than between the same period of 2020. In terms of correlations,
515 PC4 is only correlated to BOA at -2 m and -1 m ($r = 0.54$ and 0.52 , respectively), correlation values
516 then decrease with the elevation, under the significance threshold of 0.5, which confirms our
517 previous observations.

518 *PC 5 – Beach cell rotation*

519 PC5, Figure 7e, represents another longshore mechanism of rotation, this time influenced by the
520 presence of groin structures. Indeed, the left beach cell - bounded by Groins 1 and 2 - is divided into
521 mainly two lateral compartments, the left one of which follows the dynamics of the area located on
522 the right side of Groin 2 (i.e., the left side of the unmonitored beach cell at the right extremity).

523 The stability line adopts the same shape as the one of PC4, except that instead of connecting both
524 cross-shore sides, it connects between the two beach cells and forms a thin string of warmer colors
525 at elevation -1 m. This string translates the presence of a local change in the slope at the lowest
526 elevations provoked by a difference of cross-shore migration rates between elevations -1 m and -2
527 m. This phenomenon is thought to be the result of sediment by passing Groin 2, which is rarely

528 exposed to water under 0 m, contrary to Groin 1. In addition, the stability line follows the direction of
529 Groin 2, which once more highlights the influence of groins on the sediment dynamics. Similar
530 observations on a beach of North Carolina, USA were made by Miller and Dean (2007).

531 Considering the temporal evolution, $C_5(t)$ present a periodic variability with cycles from a few weeks
532 up to 3 months, that do not correspond to the ones of the larger scale rotation $C_4(t)$. Positive values
533 correspond to a clockwise orientation, while negative ones are relative to a counterclockwise
534 orientation. $C_5(t)$ is correlated with BOA at +1 m, +2 m and +3 m which is the opposite of PC4 and
535 confirms that rotation is affected by the presence of groin structures, hence the need for 2 modes to
536 describe this mechanism while including or excluding groins.

537 4.2.2. Hautot-sur-Mer

538 *PC 1 – Right centered beach cell rotation*

539 Figure 8 presents the results of the previous methodology applied to Hautot-sur-Mer. $E_1(x) \times E_1(y)$,
540 displayed in Figure 8a, opposes both left and right sides of the beach cells with a quasi-vertical
541 stability line located towards the right and a maximum of variability to the left. PC1 is therefore
542 characterizing a longshore rotation mechanism with a stability/pivot line located around transects
543 P90 and P30 for the right and left beach cells, respectively. Another cross-shore oriented stability line
544 can be seen at the position of Groin 2, which shows that this rotation mechanism is limited to the
545 beach cell spatial scale.

546 $C_1(t)$ shows a very clear seasonality pattern with negative values from April to September, and
547 positive ones from September to April, following a near binary evolution with values averaging either
548 +50 or -50, and rarely others. This situation translates the presence of two main stable shoreline
549 orientations: counterclockwise when $C_1(t)$ values are negative, and clockwise when they are
550 positive, while most states in between seem to be transitory.

551 Regarding correlations (Figure 9), PC1 shows high correlations with both BW and BOA, the first of
552 which increases with height ($r = 0.72, 0.83$ and 0.87 for +1 m, +2 m, and +3 m, respectively) when the
553 second decreases ($r = 0.88, 0.86$ and 0.84 for +1 m, +2 m, and +3 m, respectively). The reason for
554 such high correlation values with BW being related to a beach rotation mode is the unbalance in size
555 and relative variability between both sides of the cell. With a higher magnitude of variability to the

556 left and a wider region where this variability applies, losses in the left side are not fully compensated
557 by right side's gains, resulting in a rotation-induced cross-shore migration: an overall advance/retreat
558 that will be simultaneous to the rotation event (Figure 10).

559 When compared with morphodynamics, BW is the only parameter to show any significant
560 correlation, with $r = 0.53$ and 0.5 for elevations +3 m and +2 m, respectively. Regarding
561 hydrodynamics, correlation with the longshore wave energy ($r = 0.45$) and both the cross-shore and
562 total wave energy ($r = 0.39$) remain relatively high compared with other parameters despite being
563 below the significance threshold of 0.5. This tends to indicate that PC1 and more specifically its
564 cross-shore migration aspect is likely linked to wave dissipation processes.

565 *PC 2 – Left centered beach cell rotation*

566 $E_2(x) \times E_2(y)$ in Figure 8b exhibit a very similar spatial variability as PC1 although this time, the
567 stability line present at +3 m and +2 m does not go all the way down to +1 m and stops when
568 reaching the groin and is located towards the left of the beach cells with a maximum of variability to
569 the right. We interpret PC2 as the expression of a second mode of beach cell rotation mechanism,
570 less influential than PC1, especially acting at high elevations, and with a stability/pivotal line to the
571 left around P70 and P20 for the right and left beach cells, respectively. At +1 m, the shoreline
572 essentially migrates a cross-shore movement with higher magnitudes of variability towards the left of
573 the beach cells.

574 In $C_2(t)$, positive values correspond to a clockwise orientation, and negative values represent a
575 counterclockwise one. The time series does not present any remarkable pattern such as seasonality
576 or opposed binary states similar to the ones observed with PC1. When calculating correlation values
577 (Figure 9), PC2 does not show any significant relationship with the tested parameters.

578 *PC 3 – Large scale rotation*

579 $E_3(x) \times E_3(y)$ (Figure 8c) presents an opposition between the left and right sides of the monitored
580 region, with a large near zero variability area around Groin 2, which is shown by the apparent chaotic
581 behavior of the stability line, although it overall separates both left and right compartments. It
582 therefore translates a third mode of rotation mechanism, at a larger spatial scale than the previous
583 ones.

584 $C_3(t)$ does not seem to show any significant seasonality or opposed binary states either. Positive
585 values refer to a counterclockwise orientation while negative ones are relative to a clockwise one. In
586 terms of correlation, no significant link was found between PC3 and any of the tested parameters.

587 *PC 4 – Rollover*

588 PC4 presented in Figure 8d highlights a mainly cross-shore gradient of variability although the
589 stability line shown on $E_4(x) \times E_4(y)$ is not straight. This means that PC4 encapsulates information
590 about the slope and thus translates a mechanism of rollover, whose variability varies in the
591 alongshore direction, in this case within a center of rotation located at lower elevation near the
592 groins and at higher elevation around the middle of the beach cell.

593 $C_4(t)$ shows a slight seasonal alternation of negative values (gentle/dissipative slope) between May
594 and October (i.e., summer), and positive (steep/reflective slope) the rest of the time. However, the
595 minimum (most gentle slope) is reached in January 2020, i.e., during the storm period. Regarding
596 correlations, PC4 is significantly correlated with BS, which confirms our interpretation of this mode
597 being a characterization of a rollover mechanism.

598 4.3. Periods of variability and morphological response to hydrodynamic conditions

599 The temporal variability of the different shoreline's morphological parameters (BW, BOA and BS) was
600 assessed using a wavelet analysis. For each elevation, the wavelet power was temporally averaged
601 (GWS), thus highlighting the period(s) carrying the most variability. Due to the limited length of the
602 time series, only shorter periods than approximately 6 months in Hautot-sur-Mer and 8 months in
603 Etretat fell within the wavelet's cone of influence, which are therefore the longest periods to be
604 analyzed. Results are presented in Figure 11a to f. For comparison, the same analysis was performed
605 using time series of different hydrodynamic parameters including wave energy, current speeds, and
606 tidal range (Figure 11e to j). Table 3 summarizes the main periods of variability identified on Figure
607 11.

608 For both sites, most of the variability is located towards the longest periods (6 to 8 months),
609 regardless of the parameter or the elevation. Morphological variability is also depending on the
610 elevation, especially for longer periods than 5 months (Figure 11). This corresponds to the
611 observations made by multiple authors (Lemos et al., 2018; Reeve et al., 2007) although

612 investigations are usually carried out over longer timeframes (typically decades using monthly
613 measurements). Interestingly, the magnitude of BOA's variability in Etretat is not proportional to the
614 absolute elevation but rather to the relative elevation compared to the mean sea level. This
615 observation suggests that the amplitude of beach rotation is minimal towards $z = 0$ m and increases
616 at both higher and lower elevations, which was not reported in the literature, to the authors'
617 knowledge.

618 In Etretat, identified periods of morphological variability include 2, 3, 5 and 8+ months, all
619 parameters and elevations considered (Figure 11, Table 3). In Hautot-sur-Mer, periods were
620 identified at 2 and 6 months for all parameters, with an additional period at 3 months for BS alone.
621 The observed periods correspond to medium-scales components of variability, which are usually
622 related to seasonal or near-seasonal hydrodynamic processes (Loureiro and Ferreira, 2020). More
623 specifically, the wave exposure and the occurrence of storms are often documented as the main
624 process responsible for medium-term morphological changes (McCarroll et al., 2019; Ruiz de Alegria-
625 Arzaburu and Masselink, 2010; Turki et al., 2013). Hydrodynamics' spectral patterns remain very
626 similar from one site to the other. The wave energy spectrum presents two main periods at 2 and 8+
627 months in Etretat, and at 2 and 6 months in Hautot-sur-Mer. The tidal range spectrum shows two
628 main periods at 1 month and 2 weeks, the latter also being the only period identified on the current
629 speed spectrum. These periods respectively correspond to the monthly lunar (Mm, $T = 27.5$ d) and
630 the fortnightly lunar (Mf, $T = 13.6$ d) tidal components. Although tidal ranges play an essential role in
631 distributing the wave energy along beach profiles (Masselink and Short, 1993), and tidal energy
632 converted into currents is proportional to the tidal amplitude squared (Hammons, 1993),
633 investigated tidal processes do not modulate a significant part of the beaches' morphodynamical
634 variability for shorter periods than 6 to 8 months. Thus, the wave energy is the only parameter to
635 show common periods of variability with morphodynamics, meaning that wave processes are in good
636 part responsible for temporal changes of BW, BOA and BS signals. These results tend to agree with
637 findings from Stark and Hay (2016), who showed that the bottom stress of tidal currents in a mega-
638 tidal context was too low to significantly move single gravel.

639 These results provide insights regarding the processes responsible for the observed beach
640 morphodynamics but remain limited by the length and nature of available time series. Indeed, wave

641 breaking and swash were specifically shown to be linked with morphological processes especially for
642 gravel beaches (Guest and Hay, 2021) although their variability is expected to be more significant at
643 longer time scales (Almeida et al., 2014; Buscombe and Masselink, 2006; Karunaratna et al., 2012;
644 Poate et al., 2013; Ratliff and Murray, 2014).

645 4.4. Spatio-temporal variability of the surficial gravel size

646 Gravel beaches' ability to dissipate wave energy through infiltration was shown to be a function of
647 the permeability associated with the local size distribution of the gravel fabric (McCall et al., 2012,
648 2015). Other studies reported results suggesting that the surface roughness is also and maybe even
649 more important than permeability as a controlling factor of the wave energy dissipation and
650 reflection, and thus of the beaches' response to hydrodynamics (Jennings and Shulmeister, 2002;
651 Mason et al., 1997; Powell, 1990). Moreover, at each instant the mobilizable gravels on a beach are
652 expected to be the surficial ones, as they are the ones receiving most of the drag force due to waves
653 while remaining relatively free to move, which can be summarized by the concept of entrainment
654 threshold (Brayne et al., 2020; Lorang, 2000). Surficial gravels tend to get sorted by size and shape,
655 thus forming a patchwork of so called clast assemblages, each of which corresponds to a "discrete
656 population of gravel clasts which is characterized by textural unity" (Bluck, 1999). The presence of
657 assemblages on the beach face highlights the spatial variability of surface roughness (Stark et al.,
658 2014). Position, orientation, size, shape, and composition of assemblages are the result of
659 antecedent conditions of sediment supply availability, and sediment sorting processes (Buscombe
660 and Masselink, 2006). Their temporal variability could potentially be used as a proxy of surface
661 sediment transport processes, as was demonstrated by Guest and Hay (2021) using remote sensing
662 techniques applied on 14 days of high frequency video images, over a 2.7 m longshore span.

663 In this section, we aim to characterize some components of spatial and temporal variability of
664 surficial grain size at the scale of the beach cell, and to associate them with morphodynamics given a
665 relatively limited dataset composed of one map of mean grain size in Etretat (2020/06/10, Figure
666 12a) and three in Hautot-sur-Mer (2019/04/09, 2019/06/04 and 2020/06/09, Figures 12b, c and d,
667 respectively). Importantly, although variability of gravel shapes is thought to play an important role
668 in gravel system's dynamics (Buscombe and Masselink, 2006), shapes are not investigated in this

669 study. In Table 4, the commonly used grain size values related to each campaign are presented (D16,
670 D50, D84, mean size and std) along with other statistical factors.

671 4.4.1. Mean grain size

672 The mean grain size is lower in Etretat ($5.6 \text{ cm} \pm 1.7$) than Hautot-sur-Mer ($7.2 \text{ cm} \pm 2.8$ to 8.2
673 $\text{cm} \pm 2.9$). Indeed, Etretat's pebbles are resupplied less often due to the lower erosion rate of its
674 chalk cliffs (source of the flint supply), while being kept trapped on an embayed beach without the
675 protection of dissipative low tide terrace like in Hautot-sur-Mer (Costa et al., 2015). Therefore,
676 Etretat's pebble tend to shrink down through abrasion to a lower diameter that is more at the
677 equilibrium with the local conditions of higher wave energy, lower alongshore mobility and lower
678 resupply fluxes (Bertoni et al., 2012).

679 In Hautot-sur-Mer, the mean sediment size varies between $8.2 \text{ cm} \pm 0.29$ on 2019/04/09 and 7.2 cm
680 ± 2.6 , on 2019/06/04. This temporal variability corresponds to 32% change of volume in 2 months
681 (considering spheres with a diameter equivalent to the averaged measured clast' surface). A
682 temporal decrease in gravel size on beaches was documented by Bertoni et al. (2016), who measured
683 an average weight loss of almost 20% after an 8- to 10-month period, and 60% after 13 months on
684 240 retrieved marked marble pebbles, at Pisa's beach, in Italy. Considering these results, 32% of
685 volume difference due to abrasion in only two spring months seems high, especially with flint
686 material. Another explanation could be the occurrence of a local size sorting mechanism such as
687 rotation (measured rotation of 5° clockwise between the two dates) and mixing. In addition, the
688 occurrence of percolation through the oscillatory forcing of swash could have a segmentary effect by
689 burying/uncovering selected size ranges of clasts ("Brazil Nut Effect" (BNE) and "Reverse BNE"
690 (RBNE)(Nadler, 2012; Ulrich et al., 2007)).

691 4.4.2. Sedimentary patterns

692 On Figure 12, in general, the average clast length tends to increase from higher to lower elevations.
693 Two main types of sedimentary patterns can be identified on the maps, namely clast assemblages
694 and cusps, with spatial and temporal variabilities in the order of one to several centimeters.
695 Assemblages are textural zonation that can be located anywhere on the beach face and extend in any
696 direction, with a typical scale of several tens of meters. For example, a 50 m long assemblage
697 (Average size $> 10 \text{ cm}$, surrounding size $< 8 \text{ cm}$) can be seen at the bottom of the beach face in

698 Hautot-sur-Mer on 2020/06/09 (Figure 12d) and a similar one (Average size > 7 cm, surrounding size
699 < 6 cm) at the northeast side of Etretat's beach cell (Figure 12a), one day later. Such patterns, located
700 below the elevation of the last tide, were likely formed (at least partly) within hours to days,
701 depending on the antecedent conditions of wave energy. Higher elevation patterns such as the
702 accumulations at the top east corner of the beach cells of Hautot-sur-Mer are likely due to older
703 events. Groin structures seem to attract larger thus clasts forming groin assemblages at various
704 elevations, generally asymmetrically. Interestingly, assemblages in Hautot-sur-Mer are in general
705 periodic from beach cell to beach cell, which suggests that their conditions of formation are
706 influenced by the presence of groins, even at the beach cell's center.

707 Gravel cusps are described by Buscombe and Masselink (2006) as quasi-periodic topographic
708 oscillations of the shoreline provoked by swash flows, forming cross-shore extended horns with
709 coarser clasts and bays with smaller ones. Although no cusp is observed in Etretat, they are present
710 at every measured date in Hautot-sur-Mer with varying wavelengths and amplitude. Their presence
711 and characteristics seem to be largely responsible for the quality of size sorting: the more developed
712 the cusps, the poorer the sorting at the scale of the beach cell. However, despite being supposedly
713 well correlated to the swash energy (Guest and Hay, 2019; Jennings and Shulmeister, 2002), our
714 limited dataset doesn't allow to draw a strict relationship between the characteristics of cusps and
715 simultaneous incoming waves.

716 The similarity in size sorting between both sites in June 2020 (hardly visible to no visible cusps, 50 m
717 long assemblages at the bottom of the beach face) contrasts with the high temporal variability
718 evidenced in Hautot-sur-Mer. It suggests that similar wave climate led to the appearance of similar
719 spatial types of sorting patterns between groins, despite the differences in sediment supply
720 (available volume, gravel size), and general context (embayment, low tide terrace, vertical structure
721 (e.g., porosity and permeability)).

722 5. Conclusion

723 The morphological evolution of two pebble beaches including a purely gravel one in Etretat and a
724 composite one in Hautot-sur-Mer, was investigated using an Empirical Orthogonal Function (EOF)
725 analysis applied to 2 years long time series of shoreline positions at different elevations. The EOF's

726 Principal Components (PC) highlighted the existence of at least four mechanisms of shoreline change
727 including rotation, cross-shore migration, rollover and breathing. Despite their relative proximity, the
728 two beaches present different sets of modes: 88.5% of Etretat's shoreline position variability is
729 explained by cross-shore migration (PC1, 62.4%), rollover (PC2, 14.1%), breathing (PC3, 5.8%), large
730 scale rotation (PC4, 3.9%), and beach cell rotation (2.3%). The first mode could be related to a
731 rotation at the scale of the entire embayment, whose pivotal point would be located out of the
732 monitored area. The variability of Hautot-sur-Mer's shoreline position is explained at 72.2% by right-
733 centered rotation (PC1, 46.1%), left-centered rotation (PC2, 14.8%), large scale rotation (PC3, 7%)
734 and rollover (PC4, 4.3%). The interpretation of most of the PCs was confirmed when calculating
735 correlation coefficient between PCs and morphological parameters including beach width (BW),
736 beach orientation angle (BOA), and beach slope (BS). Moreover, the analysis showed that elevation
737 plays a significant role on all mechanisms of shoreline position change, and that the influence of
738 groin structures is more important in Hautot-sur-Mer where it plays a role in every single PC, than in
739 Etretat where it is only visible in PC5.

740 Comparison between time series of morphological and hydrodynamic parameters did not show any
741 significant linear correlation. The hydrodynamic data used in this study were consisting in offshore
742 waves provided by the WaveWatch 3 model, therefore non-linear nearshore transformations are not
743 taken into account which significantly limits the observed correlations. Nevertheless, a wavelet
744 analysis highlighted common temporal periods of variability at a mid-term scale including 2, 3, 5, 6
745 and 8+ months. Periods of 2, 6 and 8+ months also identified in signals of wave energy, however tidal
746 range and current speed did not share any common period of variability with the considered
747 morphodynamical parameters.

748 Analyzing the granulometric spatial dispersion of surface gravel particles was possible thanks to a
749 segmentation methodology applied to UAV-derived ortho-imagery. Gravel size was measured once in
750 Etretat, and at three different dates in Hautot-sur-Mer, allowing for some first order estimate of
751 temporal variability to be investigated on the latter site as well, under summer condition. In general,
752 both sites present different gravel size with D50 values of 5.2 cm in Etretat 7.0 cm in Hautot-sur-Mer
753 (time averaged). The spatial dispersion generally evidenced the presence of patterns such as a cross-
754 shore gradient, cusps, and clast assemblages whose periodicity from one beach cell to its neighbors

755 demonstrates the impact of groin structures. The temporal analysis highlighted differences through
756 time in both the average granulometry and the presence and position of patterns. For instance, an
757 average difference of -1 cm in all recorded sizes (mean, D16, D50 and D84) was observed between
758 April and June 2019, while the only significant morphological of the beach was its orientation (5°).
759 Possible explanations include seasonal abrasion and the presence of physical processes leading to
760 sorting such as percolation, and processes related to rotation. The influence of cusps variability on
761 the sediment distribution variability was also highlighted. As the need for a better knowledge and
762 understanding in the granulometric spatio-temporal variability is widely acknowledged by the
763 community of coastal scientists, this methodology shows promising results in this matter. However,
764 the length and sampling frequency of time series need to be improved in order to precisely
765 characterize the reciprocal relationship existing between hydrodynamics, morphodynamics and
766 sediment characteristics/transport.

767 [Data statement](#)

768 Data used in this article cannot be made publicly available for laboratory policy reasons, however
769 authors are open to privately share such data upon request.

770 [Acknowledgements](#)

771 This work is part of three projects, EC2CO INSU RGB (Response of Gravel Beaches—N°12720) run by
772 INSU (National Institute of Sciences of the Universe), SWOT 3 mC run by TOSCA/CNES (French
773 National Center of Spatial Studies), and the Raiv-Cot project funded by the Regional Council of
774 Normandy.

775 The authors wish to thank the city services of Etretat and Hautot-sur-Mer for supporting this study.
776 Additionally, authors are grateful for the editor and anonyme reviewers who took the time to
777 comment and help us improve this work.

778 [References](#)

779 6. Aarninkhof, S.G.J., Turner, I.L., Dronkers, T.D.T., Caljouw, M., Nipius, L., 2003. A video-based
780 technique for mapping intertidal beach bathymetry. *Coast. Eng.* 49, 275–289.
781 [https://doi.org/10.1016/S0378-3839\(03\)00064-4](https://doi.org/10.1016/S0378-3839(03)00064-4)

- 782 7. Almeida, L.P., Masselink, G., Russell, P., Davidson, M., McCall, R., Poate, T., 2014. Swash Zone
783 Morphodynamics of Coarse-Grained Beaches During Energetic Wave Conditions. *Coast. Eng.*
784 *Proc.* 1, 35. <https://doi.org/10.9753/icce.v34.currents.35>
- 785 8. Andriolo, U., Almeida, L.P., Almar, R., 2018. Coupling terrestrial LiDAR and video imagery to
786 perform 3D intertidal beach topography. *Coast. Eng.* 140, 232–239.
787 <https://doi.org/10.1016/j.coastaleng.2018.07.009>
- 788 9. Aubrey, D.G., 1979. Seasonal patterns of onshore/offshore sediment movement. *J. Geophys. Res.*
789 *Ocean.* 84, 6347–6354. <https://doi.org/https://doi.org/10.1029/JC084iC10p06347>
- 790 10. Austin, M.J., Masselink, G., 2006. Observations of morphological change and sediment transport
791 on a steep gravel beach. *Mar. Geol.* 229, 59–77. <https://doi.org/10.1016/j.margeo.2006.02.003>
- 792 11. Bertoni, D., Sarti, G., Benelli, G., Pozzebon, A., 2012. In situ abrasion of marked pebbles on two
793 coarse-clastic beaches (Marina di Pisa, Italy). *Ital. J. Geosci.* 131, 205–214.
794 <https://doi.org/10.3301/IJG.2012.04>
- 795 12. Bertoni, D., Sarti, G., Grottoli, E., Ciavola, P., Pozzebon, A., Domokos, G., Novák-Szabó, T., 2016.
796 Impressive abrasion rates of marked pebbles on a coarse-clastic beach within a 13-month
797 timespan. *Mar. Geol.* 381, 175–180. <https://doi.org/10.1016/j.margeo.2016.09.010>
- 798 13. Blossier, B., Bryan, K.R., Daly, C.J., Winter, C., 2017. Shore and bar cross-shore migration,
799 rotation, and breathing processes at an embayed beach. *J. Geophys. Res. Earth Surf.* 122, 1745–
800 1770. <https://doi.org/10.1002/2017JF004227>
- 801 14. Bluck, B.J., 1999. Clast assembling, bed-forms and structure in gravel beaches. *Trans. R. Soc.*
802 *Edinburgh, Earth Sci.* 89, 291–323. <https://doi.org/10.1017/s026359330000242x>
- 803 15. Bluck, B.J., 1967. Sedimentation of Beach Gravels: Examples from South Wales. *SEPM J.*
804 *Sediment. Res.* Vol. 37, 128–156. [https://doi.org/10.1306/74d71672-2b21-11d7-](https://doi.org/10.1306/74d71672-2b21-11d7-8648000102c1865d)
805 [8648000102c1865d](https://doi.org/10.1306/74d71672-2b21-11d7-8648000102c1865d)
- 806 16. Bonnefille, R., 1968. Contribution théorique et expérimentale à l'étude du régime des marées.
807 Université de Grenoble.
- 808 17. Brayne, R.P., Lorang, M.S., Naylor, L.A., Reinhardt, L., 2020. Field-based observation of the
809 entrainment threshold of cobbles with motion loggers. *J. Coast. Res.* 95, 392–397.
- 810 18. Buscombe, D., Masselink, G., 2006. Concepts in gravel beach dynamics. *Earth-Science Rev.* 79,
811 33–52. <https://doi.org/10.1016/j.earscirev.2006.06.003>

- 812 19. Castelle, B., Bujan, S., Marieu, V., Ferreira, S., 2020. 16 Years of Topographic Surveys of Rip-
813 Channelled High-Energy Meso-Macrotidal Sandy Beach. *Sci. Data* 7.
814 <https://doi.org/10.1038/s41597-020-00750-5>
- 815 20. Chabert D'Hières, G., Le Provost, C., 1978. Atlas des composantes harmoniques de la marée dans
816 la Manche. *Ann. Hydrogr.* 6.
- 817 21. Chassignet, E.P., Hurlburt, H.E., Smedstad, O.M., Halliwell, G.R., Hogan, P.J., Wallcraft, A.J.,
818 Baraille, R., Bleck, R., 2007. The HYCOM (HYbrid Coordinate Ocean Model) data assimilative
819 system. *J. Mar. Syst.* 65, 60–83. <https://doi.org/10.1016/j.jmarsys.2005.09.016>
- 820 22. Costa, S., Letortu, P., Laignel, B., 2015. The Hydro-sedimentary System of the Upper-Normandy
821 Coast: Synthesis BT - Sediment Fluxes in Coastal Areas, in: Maanan, M., Robin, M. (Eds.), .
822 Springer Netherlands, Dordrecht, pp. 121–147. https://doi.org/10.1007/978-94-017-9260-8_6
- 823 23. Davidson, M., Van Koningsveld, M., de Kruif, A., Rawson, J., Holman, R., Lamberti, A., Medina, R.,
824 Kroon, A., Aarninkhof, S., 2007. The CoastView project: Developing video-derived Coastal State
825 Indicators in support of coastal zone management. *Coast. Eng.* 54, 463–475.
826 <https://doi.org/10.1016/j.coastaleng.2007.01.007>
- 827 24. Dumas, F., Pineau-Guillou, L., Lecornu, F., Le Roux, J.-F., Le Squère, B., 2014. General
828 Introduction: PREVIMER, a French pre-operational coastal ocean forecasting capability. *Mercat.*
829 *Ocean.*
- 830 25. Flemming, N.C., 1964. Tank experiments on the sorting of beach material during cusp formation.
831 *Bull. Japan Inst. Met.* 3, 249–258.
- 832 26. Guest, T.B., Hay, A.E., 2021. Small-scale morpho-sedimentary dynamics in the swash zone of a
833 megatidal mixed sand–gravel beach. *J. Mar. Sci. Eng.* 9. <https://doi.org/10.3390/jmse9040413>
- 834 27. Guest, T.B., Hay, A.E., 2019. Timescales of beach cusp evolution on a steep, megatidal, mixed
835 sand-gravel beach. *Mar. Geol.* 416, 105984. <https://doi.org/10.1016/J.MARGE0.2019.105984>
- 836 28. Hammons, T.J., 1993. Tidal Power. *Proc. IEEE* 81, 419–433. <https://doi.org/10.1109/5.241486>
- 837 29. Hapke, C.J., Plant, N.G., Henderson, R.E., Schwab, W.C., Nelson, T.R., 2016. Decoupling processes
838 and scales of shoreline morphodynamics. *Mar. Geol.* 381, 42–53.
839 <https://doi.org/10.1016/j.margeo.2016.08.008>
- 840 30. Harley, M.D., Turner, I.L., Short, A.D., 2015. New insights into embayed beach rotation: The
841 importance of wave exposure and cross-shore processes. *J. Geophys. Res. F Earth Surf.* 120,

- 842 1470–1484. <https://doi.org/10.1002/2014JF003390>
- 843 31. Hay, A.E., Zedel, L., Stark, N., 2014. Sediment dynamics on a steep, megatidal, mixed sand-gravel-
844 cobble beach. *Earth Surf. Dyn.* 2, 443–453. <https://doi.org/10.5194/esurf-2-443-2014>
- 845 32. He, K., Gkioxari, G., Dollar, P., Girshick, R., 2017. Mask R-CNN. *Proc. IEEE Int. Conf. Comput. Vis.*
846 2017-October, 2980–2988. <https://doi.org/10.1109/ICCV.2017.322>
- 847 33. Holman, R.A., Stanley, J., 2007. The history and technical capabilities of Argus. *Coast. Eng.* 54,
848 477–491. <https://doi.org/10.1016/j.coastaleng.2007.01.003>
- 849 34. Isla, F.I., 1993. Overpassing and armouring phenomena on gravel beaches. *Mar. Geol.* 110, 369–
850 376. [https://doi.org/10.1016/0025-3227\(93\)90094-C](https://doi.org/10.1016/0025-3227(93)90094-C)
- 851 35. Isla, F.I., Bujalesky, G.G., 2000. Cannibalisation of Holocene gravel beach-ridge plains, northern
852 Tierra del Fuego, Argentina. *Mar. Geol.* 170, 105–122. [https://doi.org/10.1016/S0025-](https://doi.org/10.1016/S0025-3227(00)00069-4)
853 [3227\(00\)00069-4](https://doi.org/10.1016/S0025-3227(00)00069-4)
- 854 36. Jennings, R., Shulmeister, J., 2002. A field based classification scheme for gravel beaches. *Mar.*
855 *Geol.* 186, 211–228. [https://doi.org/10.1016/S0025-3227\(02\)00314-6](https://doi.org/10.1016/S0025-3227(02)00314-6)
- 856 37. Karunarathna, H., Horrillo-Caraballo, J., Ranasinghe, R., Short, A., Reeve, D., 2012. An analysis the
857 of cross-shore beach morphodynamics of a sandy and a composite gravel beaches. *Coast. Eng.*
858 *Proc.* 1, 18. <https://doi.org/10.9753/icce.v33.sediment.18>
- 859 38. Karunarathna, H., Pender, D., Ranasinghe, R., Short, A.D., Reeve, D.E., 2014. The effects of storm
860 clustering on beach profile variability. *Mar. Geol.* 348, 103–112.
861 <https://doi.org/10.1016/j.margeo.2013.12.007>
- 862 39. Krumbein, W.C., Monk, G.D., 1943. Permeability as a Function of the Size Parameters of
863 Unconsolidated Sand. *Trans. AIME* 151, 153–163. <https://doi.org/10.2118/943153-g>
- 864 40. Lacey, E.M., Peck, J.A., 1998. Long-term beach profile variations along the south shore of Rhode
865 Island, U.S.A. *J. Coast. Res.* 14, 1255–1264.
- 866 41. Larson, M., Kraus, N.C., 1994. Temporal and spatial scales of beach profile change, Duck, North
867 Carolina. *Mar. Geol.* 117, 75–94. [https://doi.org/10.1016/0025-3227\(94\)90007-8](https://doi.org/10.1016/0025-3227(94)90007-8)
- 868 42. Lee, J.-M., Park, J.-Y., Choi, J.-Y., 2013. Evaluation of Sub-aerial Topographic Surveying Techniques
869 Using Total Station and RTK-GPS for Applications in Macrotidal Sand Beach Environment. *J. Coast.*
870 *Res.* 65, 535–540. <https://doi.org/10.2112/si65-091.1>
- 871 43. Lemke, L., Miller, J.K., 2017. EOF analysis of shoreline and beach slope variability at a feeder

872 beach constructed within a groin field at Long Branch, New Jersey. *Coast. Eng.* 121, 14–25.
873 <https://doi.org/10.1016/j.coastaleng.2016.11.001>

874 44. Lemos, C., Floc'h, F., Yates, M., Le Dantec, N., Marieu, V., Hamon, K., Cuq, V., Suanez, S.,
875 Delacourt, C., 2018. Equilibrium modeling of the beach profile on a macrotidal embayed low tide
876 terrace beach. *Ocean Dyn.* 68, 1207–1220. <https://doi.org/10.1007/s10236-018-1185-1>

877 45. Leont'yev, I.O., 2018. Changes in shoreline contour due to cross-shore structure in the Sea
878 Coastal Zone. *Geomorfologiya 2018-Janua*, 32–39. <https://doi.org/10.7868/S0435428118030033>

879 46. Leont'yev, I.O., 2007. Changes in the shoreline caused by coastal structures. *Oceanology* 47, 877–
880 883. <https://doi.org/10.1134/S0001437007060124>

881 47. Levoy, F., Anthony, E.J., Monfort, O., Larssonneur, C., 2000. The morphodynamics of megatidal
882 beaches in Normandy, France. *Mar. Geol.* 171, 39–59. [https://doi.org/10.1016/S0025-](https://doi.org/10.1016/S0025-3227(00)00110-9)
883 [3227\(00\)00110-9](https://doi.org/10.1016/S0025-3227(00)00110-9)

884 48. Lorang, M.S., 2000. Predicting threshold entrainment mass for a boulder beach. *J. Coast. Res.* 16,
885 432–445.

886 49. Loureiro, C., Ferreira, Ó., 2020. Mechanisms and timescales of beach rotation, Sandy Beach
887 Morphodynamics. Elsevier Ltd. <https://doi.org/10.1016/b978-0-08-102927-5.00024-2>

888 50. Mason, D.C., Gurney, C., Kennett, M., 2000. Beach topography mapping - a comparison of
889 techniques. *J. Coast. Conserv.* 6, 113–124. <https://doi.org/10.1007/BF02730475>

890 51. Mason, T., Coates, T.T., 2001. Sediment transport processes on mixed beaches: A review for
891 shoreline management. *J. Coast. Res.* 17, 645–657.

892 52. Mason, T., Voulgaris, G., Simmonds, D.J., Collins, M.B., 1997. Hydrodynamics and sediment
893 transport on composite (mixed sand/shingle) and sand beaches: A comparison, in: *Coastal*
894 *Dynamics' 97*. ASCE, pp. 48–57.

895 53. Masselink, G., Short, A.D., 1993. The effect of tide range on beach morphodynamics and
896 morphology: a conceptual beach model. *J. Coast. Res.* 9, 785–800.

897 54. McCall, R., Masselink, G., Roelvink, D., Russel, P., Davidson, M., Poate, T., 2012. MODELLING
898 OVERWASH AND INFILTRATION ON GRAVEL BARRIERS. *Coast. Eng.* 33, 1–15.
899 [https://doi.org/doi.org/10.9753/icce.v33.currents.34](https://doi.org/10.9753/icce.v33.currents.34)

900 55. McCall, R.T., Masselink, G., Poate, T.G., Roelvink, J.A., Almeida, L.P., 2015. Modelling the
901 morphodynamics of gravel beaches during storms with XBeach-G. *Coast. Eng.* 103, 52–66.

- 902 <https://doi.org/10.1016/j.coastaleng.2015.06.002>
- 903 56. McCarroll, R.J., Masselink, G., Wiggins, M., Scott, T., Billson, O., Conley, D., 2019. Gravel Beach
904 Cross- and Alongshore Response To an Extreme Event: Beach Length and Headland Proximity
905 Controls 2735–2745. https://doi.org/10.1142/9789811204487_0234
- 906 57. Medina, R., Losada, M.A., Losada, I.J., Vidal, C., 1994. Temporal and spatial relationship between
907 sediment grain size and beach profile. *Mar. Geol.* 118, 195–206. [https://doi.org/10.1016/0025-](https://doi.org/10.1016/0025-3227(94)90083-3)
908 [3227\(94\)90083-3](https://doi.org/10.1016/0025-3227(94)90083-3)
- 909 58. Medina, R., Vidal, C., Losada, M.A., Roldan, A.J., 1993. Three-mode principal component analysis
910 of bathymetric data, applied to " Playa de Castilla"(Huelva, Spain), in: *Coastal Engineering 1992*.
911 pp. 2265–2278.
- 912 59. Michaud, H., Pasquet, A., Baraille, R., Leckler, F., Aouf, L., Dalphiné, A., Huchet, M., Roland, A.,
913 Dutour-Sikirić, M., Arduin, F., others, Dutour Sikirić, M., Arduin, F., Filipot, J.-F., 2015.
914 Implementation of the new French operational coastal wave forecasting system and application
915 to a wave-current interaction study, in: *14th International Workshop on Wave Hindcasting and*
916 *Forecasting, and 5 Coastal Hazard Symposium*.
- 917 60. Miller, J.K., Dean, R.G., 2007. Shoreline variability via empirical orthogonal function analysis: Part
918 I temporal and spatial characteristics. *Coast. Eng.* 54, 111–131.
919 <https://doi.org/10.1016/j.coastaleng.2006.08.013>
- 920 61. Montaña, J., Coco, G., Antolínez, J.A.A., Beuzen, T., Bryan, K.R., Cagigal, L., Castelle, B., Davidson,
921 M.A., Goldstein, E.B., Ibaceta, R., Idier, D., Ludka, B.C., Masoud-Ansari, S., Méndez, F.J., Murray,
922 A.B., Plant, N.G., Ratliff, K.M., Robinet, A., Rueda, A., Sénéchal, N., Simmons, J.A., Splinter, K.D.,
923 Stephens, S., Townend, I., Vitousek, S., Vos, K., 2020. Blind testing of shoreline evolution models.
924 *Sci. Rep.* 10, 1–10. <https://doi.org/10.1038/s41598-020-59018-y>
- 925 62. Morton, R.A., Leach, M.P., Paine, J.G., Cardoza, M.A., Mortont, R.A., Leacht, M.P., Painet, J.G.,
926 Car, M.A., 1993. Monitoring Beach Changes Using GPS Surveying Te stability and rates of
927 shoreline movement , which. *J. Coast. Res.* 9, 702–720.
- 928 63. Nadler, S., 2012. Comportement d ' un milieu granulaire soumis ` a des vibrations horizontales :
929 Etudes num ´ eriques et exp ´ erimentales ebastien Nadler To cite this version : Ecole Nationale
930 Supérieure des Mines de Saint-Etienne.
- 931 64. Odezulu, C.I., Lorenzo-Trueba, J., Wallace, D.J., Anderson, J.B., 2018. Follets Island: A case of

932 unprecedented change and transition from rollover to subaqueous shoals. *Barrier Dyn. Response*
933 to *Chang. Clim.* 147–174. https://doi.org/10.1007/978-3-319-68086-6_5

934 65. Orford, J.D., 1975. Discrimination of particle zonation on a pebble beach. *Sedimentology* 22, 441–
935 463. <https://doi.org/10.1111/j.1365-3091.1975.tb01640.x>

936 66. Pasquet, A., Michaud, H., Aouf, L., Baraille, R., Bru, C., Correard, S., Gouillon, F., Jourdan, D.,
937 Morvan, G., Ohl, P., Paradis, D., 2014. Implémentation d'un nouveau modèle opérationnel de
938 prévision des vagues et surcotes marines, in: *Acte Des XIIIèmes Journées Nationales Génie*
939 *Côtier-Génie Civil, Dunkerque, France. Dunkerque, France.*
940 <https://doi.org/10.5150/jngcgc.2014.017>

941 67. Plant, N.G., Aarninkhof, S.G.J., Turner, I.L., Kingston, K.S., 2007. The performance of shoreline
942 detection models applied to video imagery. *J. Coast. Res.* 23, 658–670.
943 [https://doi.org/10.2112/1551-5036\(2007\)23\[658:TPOSDM\]2.0.CO;2](https://doi.org/10.2112/1551-5036(2007)23[658:TPOSDM]2.0.CO;2)

944 68. Poate, T., Masselink, G., Davidson, M., McCall, R., Russell, P., Turner, I., 2013. High frequency in-
945 situ field measurements of morphological response on a fine gravel beach during energetic wave
946 conditions. *Mar. Geol.* 342, 1–13. <https://doi.org/10.1016/j.margeo.2013.05.009>

947 69. Powell, K.A., 1990. Predicting short term profile response for shingle beaches. *Hydraulics*
948 *Research Wallingford.*

949 70. Ratliff, K.M., Murray, A.B., 2014. Modes and emergent time scales of embayed beach dynamics.
950 *Geophys. Res. Lett.* 41, 7270–7275. <https://doi.org/10.1002/2014GL061680>

951 71. Reeve, D., Li, Y., Lark, M., Simmonds, D., 2007. An investigation of the multi-scale temporal
952 variability of beach profiles at Duck using wavelet packet transforms. *Coast. Eng.* 54, 401–415.
953 <https://doi.org/10.1016/j.coastaleng.2006.11.008>

954 72. Robinet, A., Castelle, B., Idier, D., Harley, M.D., Splinter, K.D., 2020. Controls of local geology and
955 cross-shore/longshore processes on embayed beach shoreline variability. *Mar. Geol.* 422,
956 106118. <https://doi.org/10.1016/j.margeo.2020.106118>

957 73. Ruiz de Alegria-Arzaburu, A., Masselink, G., 2010. Storm response and beach rotation on a gravel
958 beach, Slapton Sands, U.K. *Mar. Geol.* 278, 77–99. <https://doi.org/10.1016/j.margeo.2010.09.004>

959 74. Salameh, E., Frappart, F., Almar, R., Baptista, P., Heygster, G., Lubac, B., Raucoules, D., Almeida,
960 L.P., Bergsma, E.W.J., Capo, S., De Michele, M.D., Idier, D., Li, Z., Marieu, V., Poupardin, A., Silva,
961 P.A., Turki, I., Laignel, B., 2019. Monitoring Beach Topography and Nearshore Bathymetry Using

962 Spaceborne Remote Sensing: A Review. *Remote Sens.* 11. <https://doi.org/10.3390/rs11192212>

963 75. SHOM, 1953. Les courants de marée dans la mer de la Manche et sur les côtes françaises de
964 l'Atlantique. Service Hydrographique et Océanographique de la Marine, Paris.

965 76. Short, A.D., Trembanis, A.C., Turner, I.L., 2000. Beach oscillation, rotation and the Southern
966 Oscillation, Narrabeen Beach, Australia. *Coast. Eng.* 2000 - Proc. 27th Int. Conf. Coast. Eng. ICCE
967 2000 276. [https://doi.org/10.1061/40549\(276\)191](https://doi.org/10.1061/40549(276)191)

968 77. Silva, A.N., Taborda, R., Catalão, J., Freire, P., 2009. DTM extraction using video-monitoring
969 techniques: Application to a fetch limited beach. *J. Coast. Res.* 1, 203–207.

970 78. Soloy, A., Turki, I., Fournier, M., Costa, S., Peuziat, B., Lecoq, N., 2020. A deep learning-based
971 method for quantifying and mapping the grain size on pebble beaches. *Remote Sens.* 12, 1–23.
972 <https://doi.org/10.3390/rs12213659>

973 79. Soloy, A., Turki, I., Lecoq, N., Gutiérrez Barceló, Á.D., Costa, S., Laignel, B., Bazin, B., Soufflet, Y.,
974 Le Louargant, L., Maquaire, O., 2021. A fully automated method for monitoring the intertidal
975 topography using Video Monitoring Systems. *Coast. Eng.* 103894.
976 <https://doi.org/10.1016/j.coastaleng.2021.103894>

977 80. Stark, N., Hay, A.E., 2016. Pebble and cobble transport on a steep, mega-tidal, mixed sand and
978 gravel beach. *Mar. Geol.* 382, 210–223. <https://doi.org/10.1016/j.margeo.2016.10.012>

979 81. Stark, N., Hay, A.E., Cheel, R., Lake, C.B., 2014. The impact of particle shape on the angle of
980 internal friction and the implications for sediment dynamics at a steep, mixed sand-gravel beach.
981 *Earth Surf. Dyn.* 2, 469–480. <https://doi.org/10.5194/esurf-2-469-2014>

982 82. Talavera, L., Río, L. Del, Benavente, J., Barbero, L., López-Ramírez, J.A., 2018. UAS & SfM-based
983 approach to Monitor Overwash Dynamics and Beach Evolution in a Sandy Spit. *J. Coast. Res.* 85,
984 221–225. <https://doi.org/10.2112/SI85-045.1>

985 83. Tolman, H.L., 2009. User manual and system documentation of WAVEWATCH-IIIITM version 3.14.
986 Tech. note 220.

987 84. Turki, I., Medina, R., Gonzalez, M., Coco, G., 2013. Natural variability of shoreline position:
988 Observations at three pocket beaches. *Mar. Geol.* 338, 76–89.
989 <https://doi.org/10.1016/j.margeo.2012.10.007>

990 85. Turner, I.L., Aarninkhof, S.G.J., Dronkers, T.D.T., McGrath, J., 2004. CZM applications of argus
991 coastal imaging at the Gold Coast, Australia. *J. Coast. Res.* 20, 739–752.

992 [https://doi.org/10.2112/1551-5036\(2004\)20\[739:caoaci\]2.0.co;2](https://doi.org/10.2112/1551-5036(2004)20[739:caoaci]2.0.co;2)

993 86. Turner, I.L., Harley, M.D., Short, A.D., Simmons, J.A., Bracs, M.A., Phillips, M.S., Splinter, K.D.,
994 2016. A multi-decade dataset of monthly beach profile surveys and inshore wave forcing at
995 Narrabeen, Australia. *Sci. Data* 3, 1–13. <https://doi.org/10.1038/sdata.2016.24>

996 87. Ulrich, S., Schröter, M., Swinney, H.L., 2007. Influence of friction on granular segregation. *Phys.*
997 *Rev. E* 76, 24–26. <https://doi.org/10.1103/physreve.76.042301>

998 88. Uunk, L., Wijnberg, K.M., Morelissen, R., 2010. Automated mapping of the intertidal beach
999 bathymetry from video images. *Coast. Eng.* 57, 461–469.
1000 <https://doi.org/10.1016/j.coastaleng.2009.12.002>

1001 89. Van Wellen, E., Chadwick, A.J., Mason, T., 2000. A review and assessment of longshore sediment
1002 transport equations for coarse-grained beaches. *Coast. Eng.* 40, 243–275.
1003 [https://doi.org/10.1016/S0378-3839\(00\)00031-4](https://doi.org/10.1016/S0378-3839(00)00031-4)

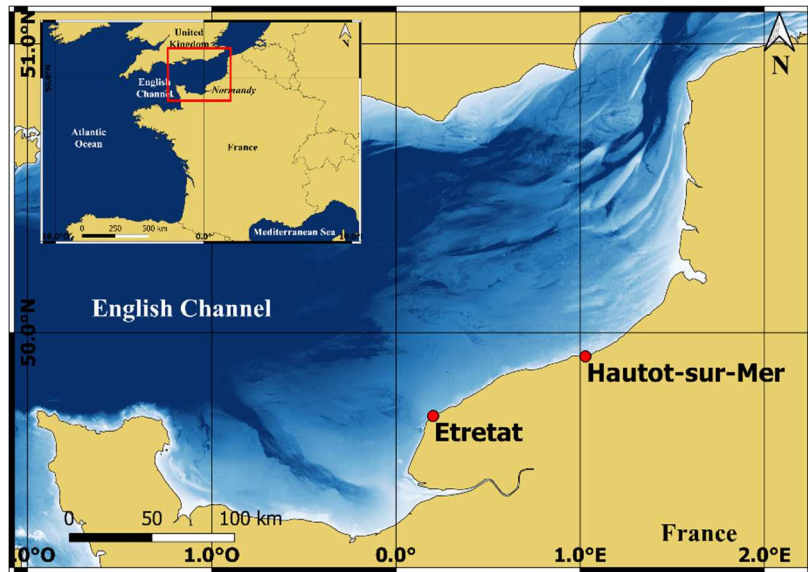
1004 90. Vos, K., Harley, M.D., Splinter, K.D., Walker, A., Turner, I.L., 2020. Beach Slopes From Satellite-
1005 Derived Shorelines. *Geophys. Res. Lett.* 47, 0–2. <https://doi.org/10.1029/2020GL088365>

1006 91. Westoby, M.J., Brasington, J., Glasser, N.F., Hambrey, M.J., Reynolds, J.M., 2012. “Structure-
1007 from-Motion” photogrammetry: A low-cost, effective tool for geoscience applications.
1008 *Geomorphology* 179, 300–314. <https://doi.org/10.1016/j.geomorph.2012.08.021>

1009 92. Williams, A.T., Caldwell, N.E., 1988. Particle size and shape in pebble-beach sedimentation. *Mar.*
1010 *Geol.* 82, 199–215. [https://doi.org/10.1016/0025-3227\(88\)90141-7](https://doi.org/10.1016/0025-3227(88)90141-7)

1011 93. Winant, C.D., Inman, D.L., Nordstrom, C.E., 1975. Description of seasonal beach changes using
1012 empirical eigenfunctions. *J. Geophys. Res.* 80, 1979–1986.
1013 <https://doi.org/https://doi.org/10.1029/JC080i015p01979>

1014



a



b



c

Figure 1 - Location maps of the study sites (a); Satellite Images of Etretat (b) and Hautot-sur-Mer (c). White frames indicate the area of interest on the beaches, the coast orientation is displayed with an arrow.

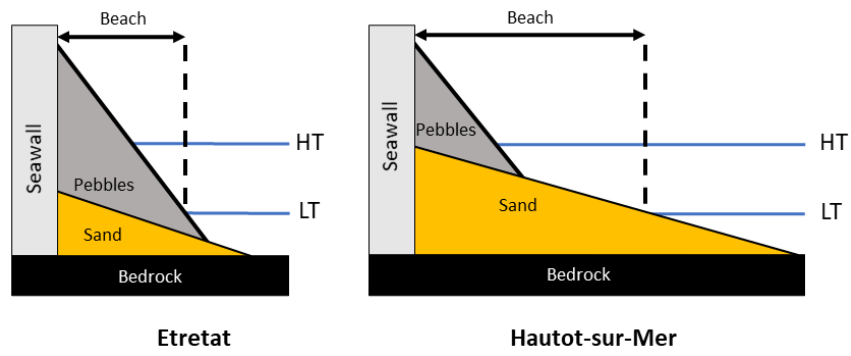


Figure 2 - Conceptual model of the cross-shore composition profile of Etretat and Hautot-sur-Mer's beaches (angles and proportions are not to scale). HT = High Tides, LT = Low Tides.

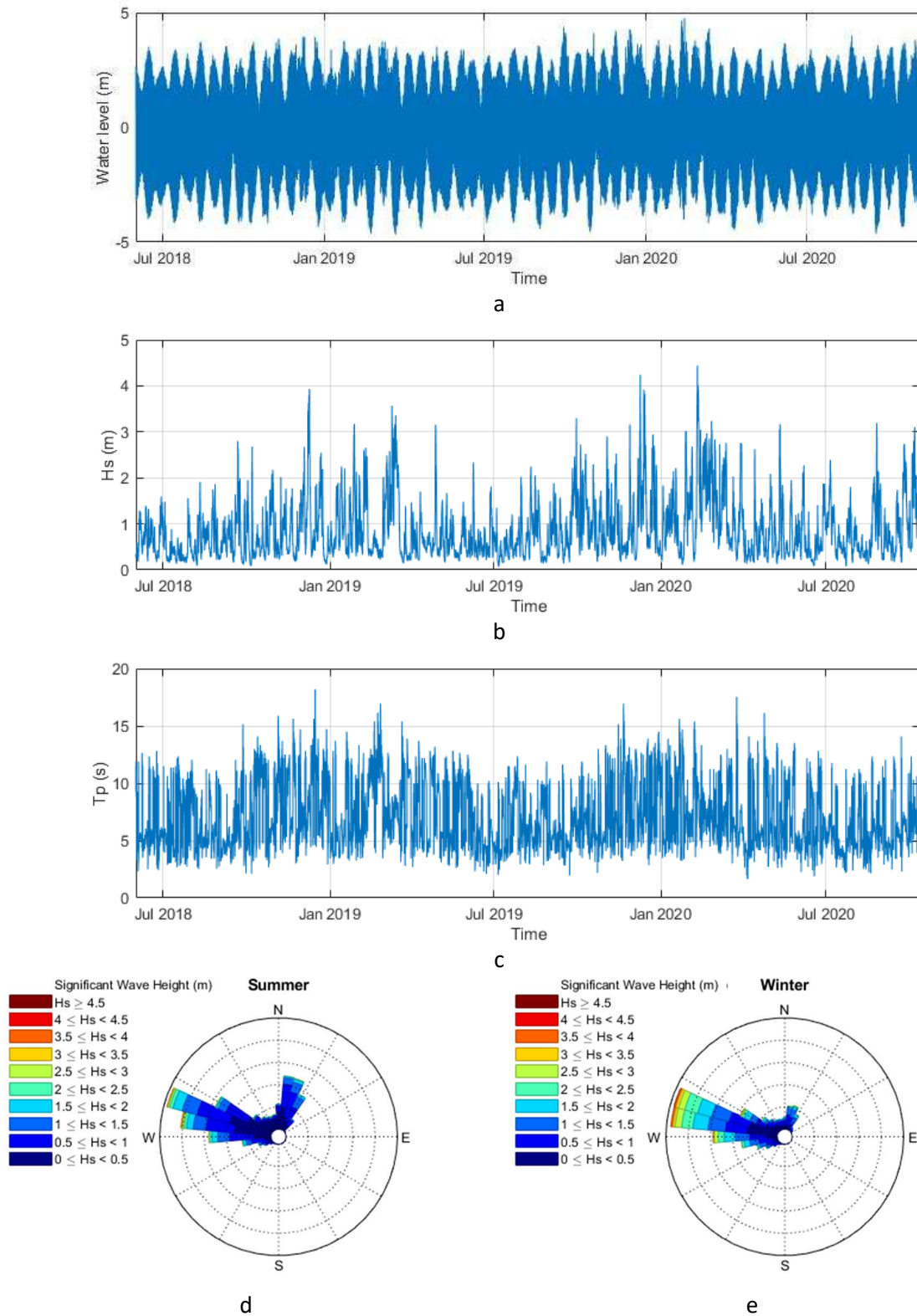


Figure 3 - Hydrodynamical parameters in Etretat from July 2018 to December 2020: Water level (datum: mean water level) (a) ; Wave Significant Height (b) ; Wave Peak Period (c) ; Roses of Wave Significant Height during Summer (April – October) (d) and Winter (October – April) (e) periods

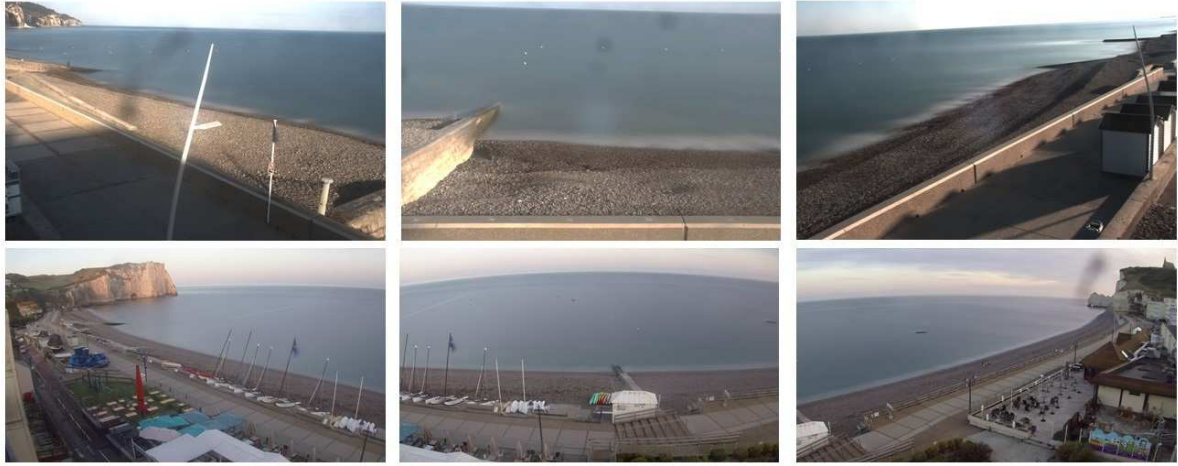


Figure 4 - Panoramic composition of the 3 camera views at Hautot-sur-Mer (top) and Etretat (bottom) (modified after Soloy et al. 2021)

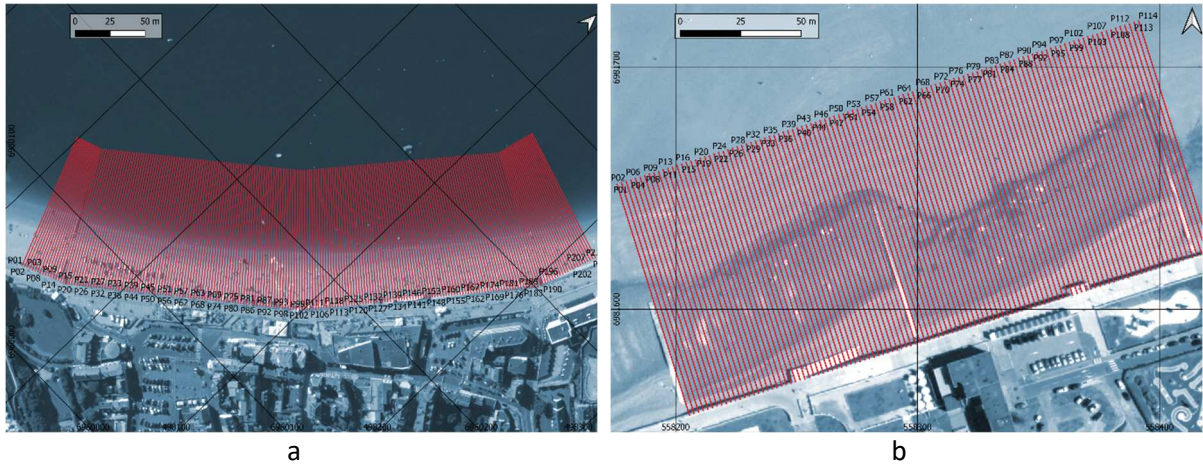


Figure 5 - Cross-shore transects used for discretizing the shoreline position along the beach of Etretat (a) and Hautot-sur-Mer (b)

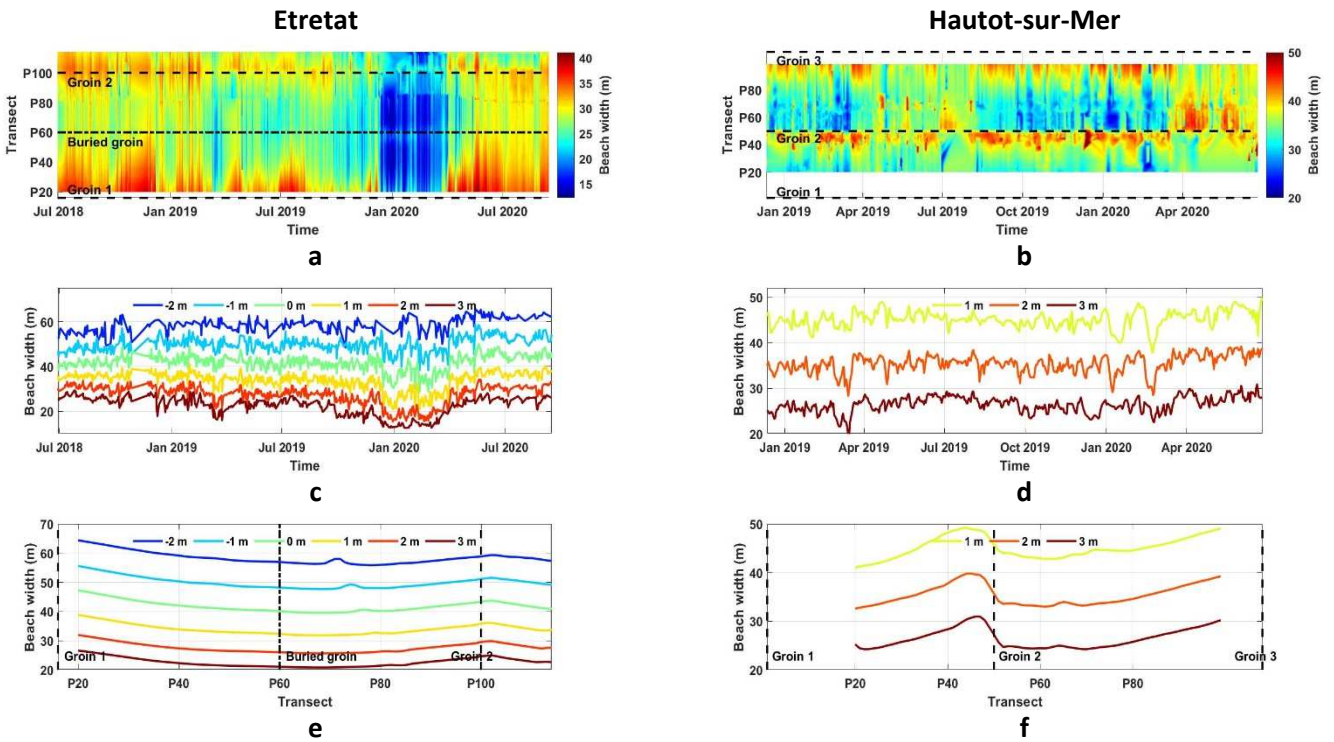


Figure 6 - Planform evolution of the +2 m elevation shoreline position at Etretat (a) and Hautot-sur-Mer (b), from July 2018 to November 2020. Time series of average beach width between elevations -2 m and +3 m in Etretat (c), and from +1 and +3 m in Hautot-sur-Mer (d), with 1 m of span. Average planform shape of the shoreline at the same elevations in Etretat (e) and Hautot-sur-Mer (f). The position of groin structures is indicated with black dashed lines.

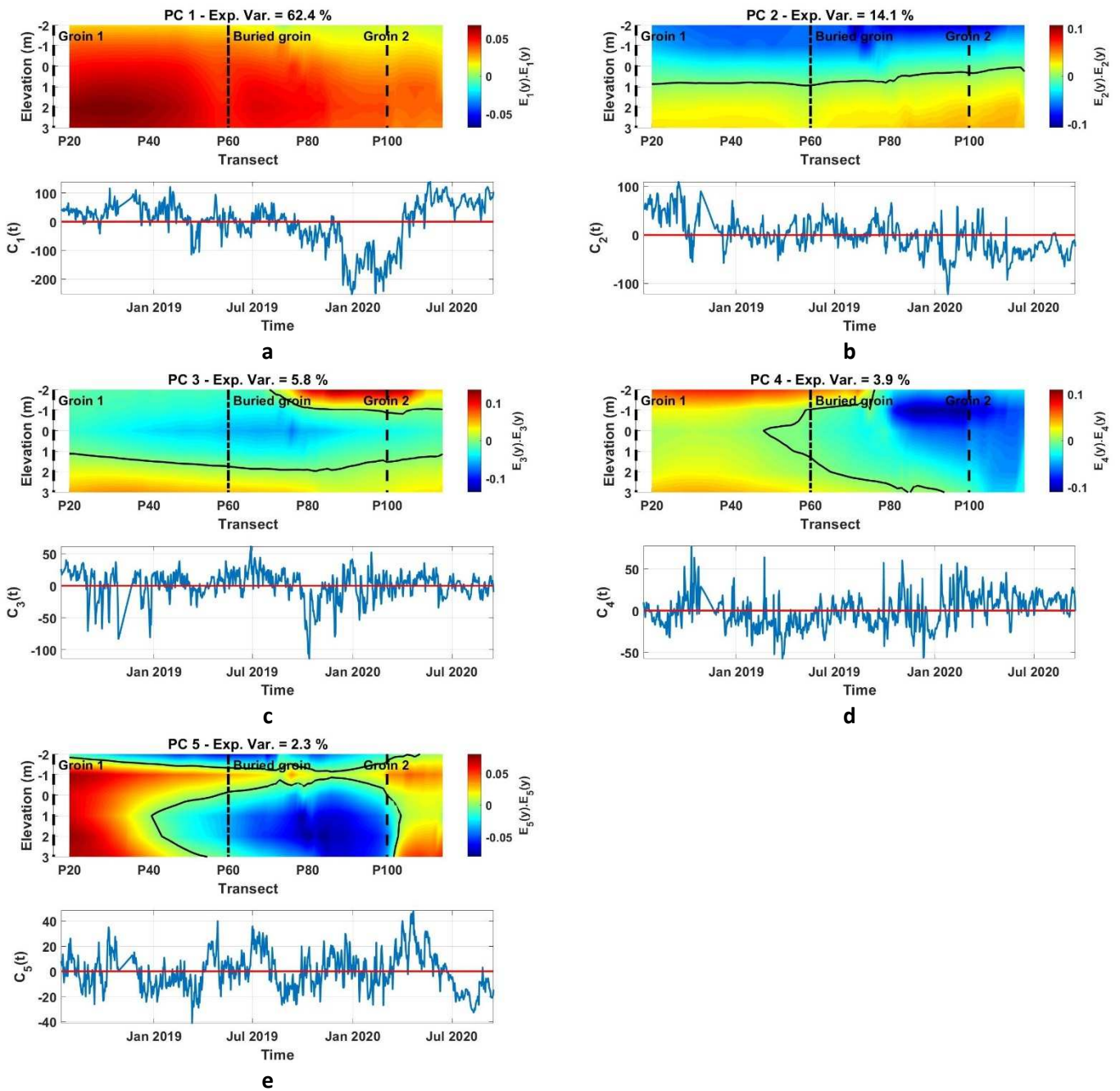


Figure 7 - Results of the EOF analysis applied to Etretat's shoreline position from elevations -2 m to +3 m. Principal Components 1 to 5 are presented in frames a to e, respectively. Top surface plots are presenting the spatial eigenfunction $E_k(x) \times E_k2(y)$, the Y axis was inverted so the sea side of is towards the figure's top and the land side is towards the bottom. Groin structures were marked with black dashed lines, and the contour of zero variability (i.e. stability line) was drawn as a solid black line. Bottom time series show the temporal eigenfunction $C_k(t)$ associated with each component, the red line highlights the minimum of variability.

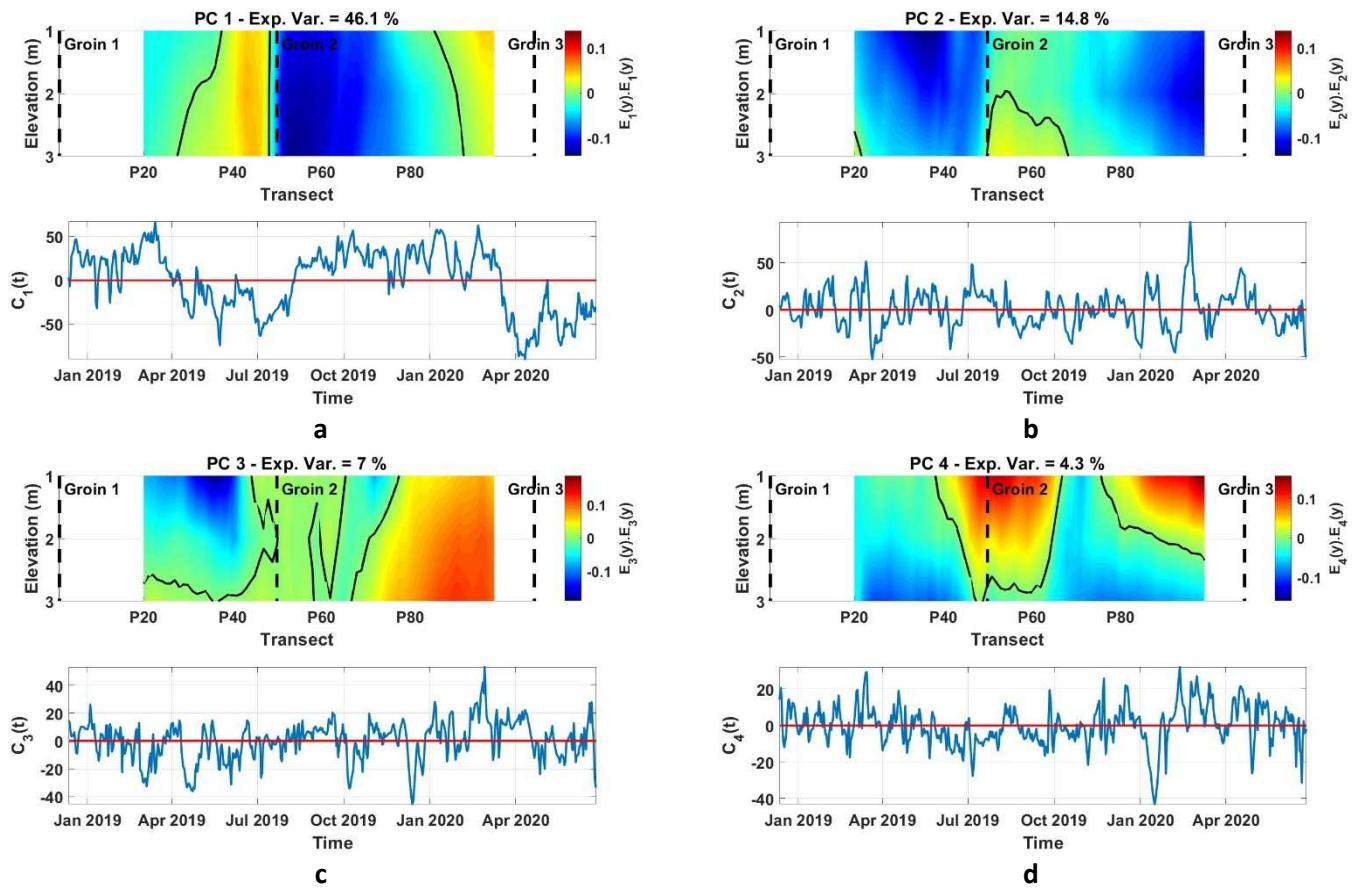


Figure 8 - Results of the EOF analysis applied to Hautot-sur-Mer's shoreline position from elevations +1 m to +3 m. Principal Components 1 to 4 are presented in frames a to d, respectively. Top surface plots are presenting the spatial eigenfunction $E_k(x) \times E_k(y)$, the Y axis was inverted so the sea side of is towards the figure's top and the land side is towards the bottom. Groin structures were marked with black dashed lines, and the contour of zero variability (i.e. stability line) was drawn as a solid black line. Bottom time series show the temporal eigenfunction $C_k(t)$ associated with each component, the red line highlights the minimum of variability.

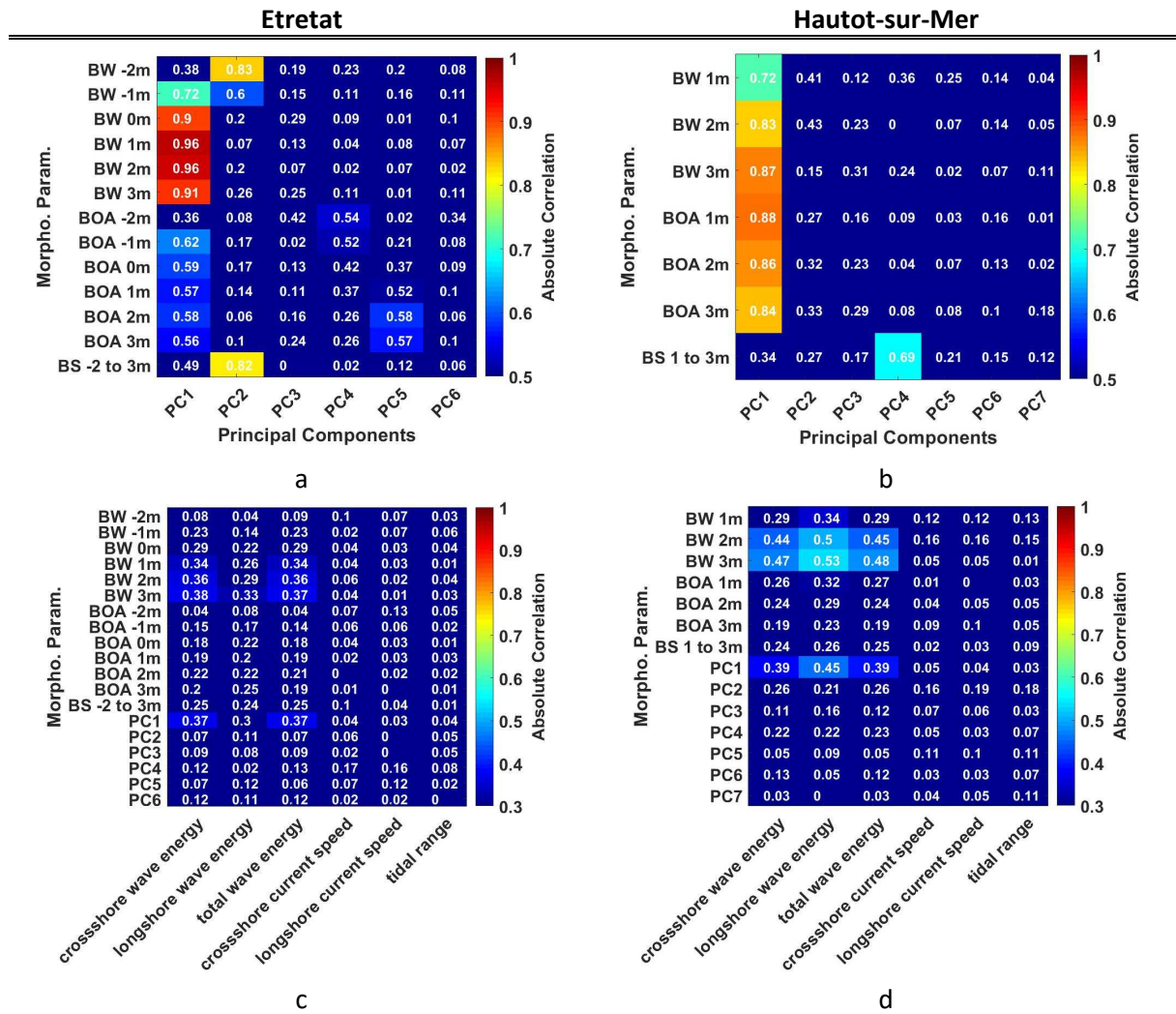
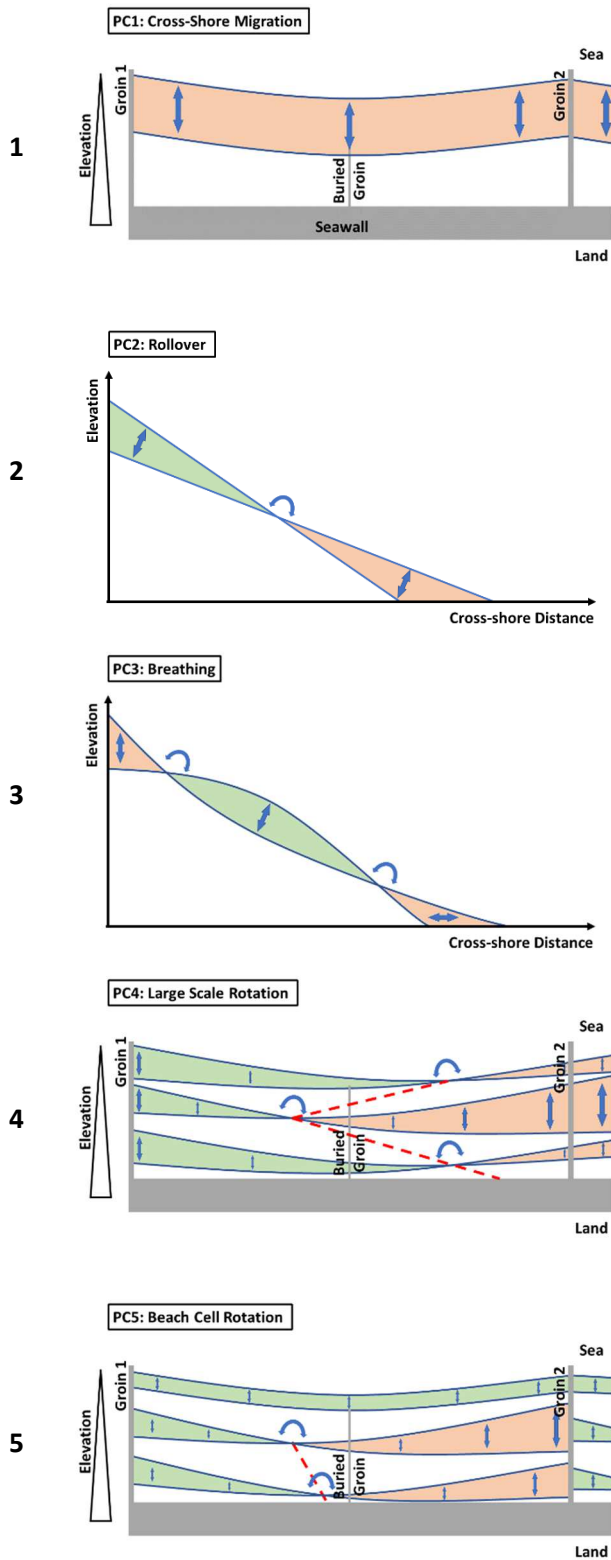


Figure 9 - Correlation matrix between morphodynamical parameters including beach width (BW), beach orientation angle (BOA) and beach slope (BS) and the temporal eigenfunction of the principal components (PC) resulting from the EOF analysis applied to Etretat's shoreline position from elevations -2 m to +3 m (a), and to Hautot-sur-Mer from elevations +1 m to +3 m (b). c and d present the same operation calculated with hydrodynamic parameters including wave energy, current speed and tidal range.

PC

Etretat



Hautot-sur-Mer

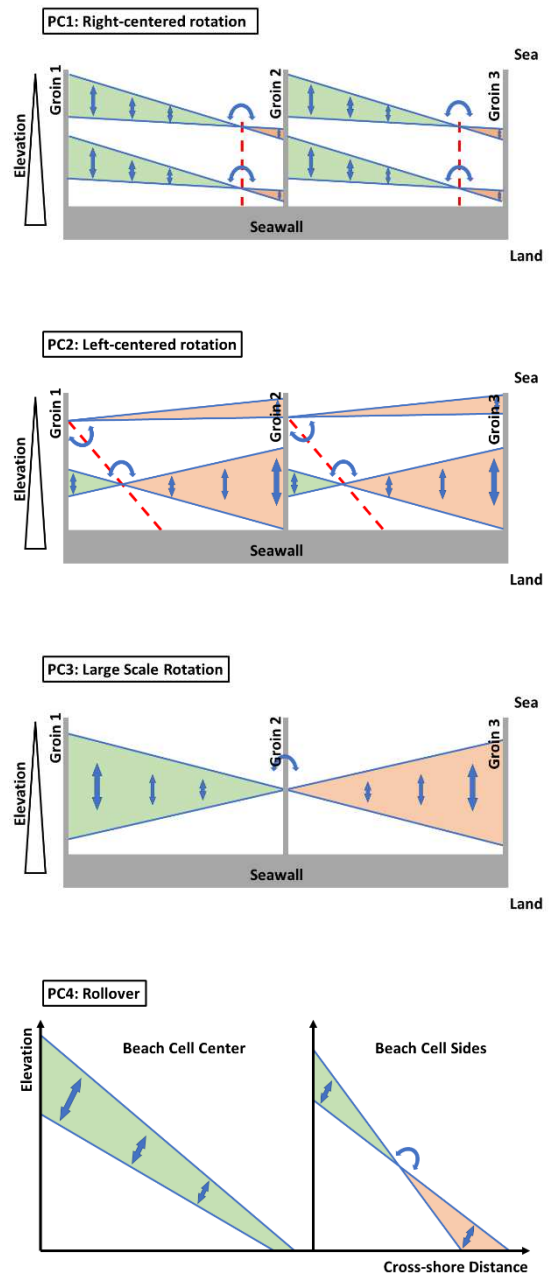


Figure 10 - Conceptual model of the isolated mechanisms of morphological variability in Etretat (left) and Hautot-sur-Mer (right), associated with their dedicated principal component

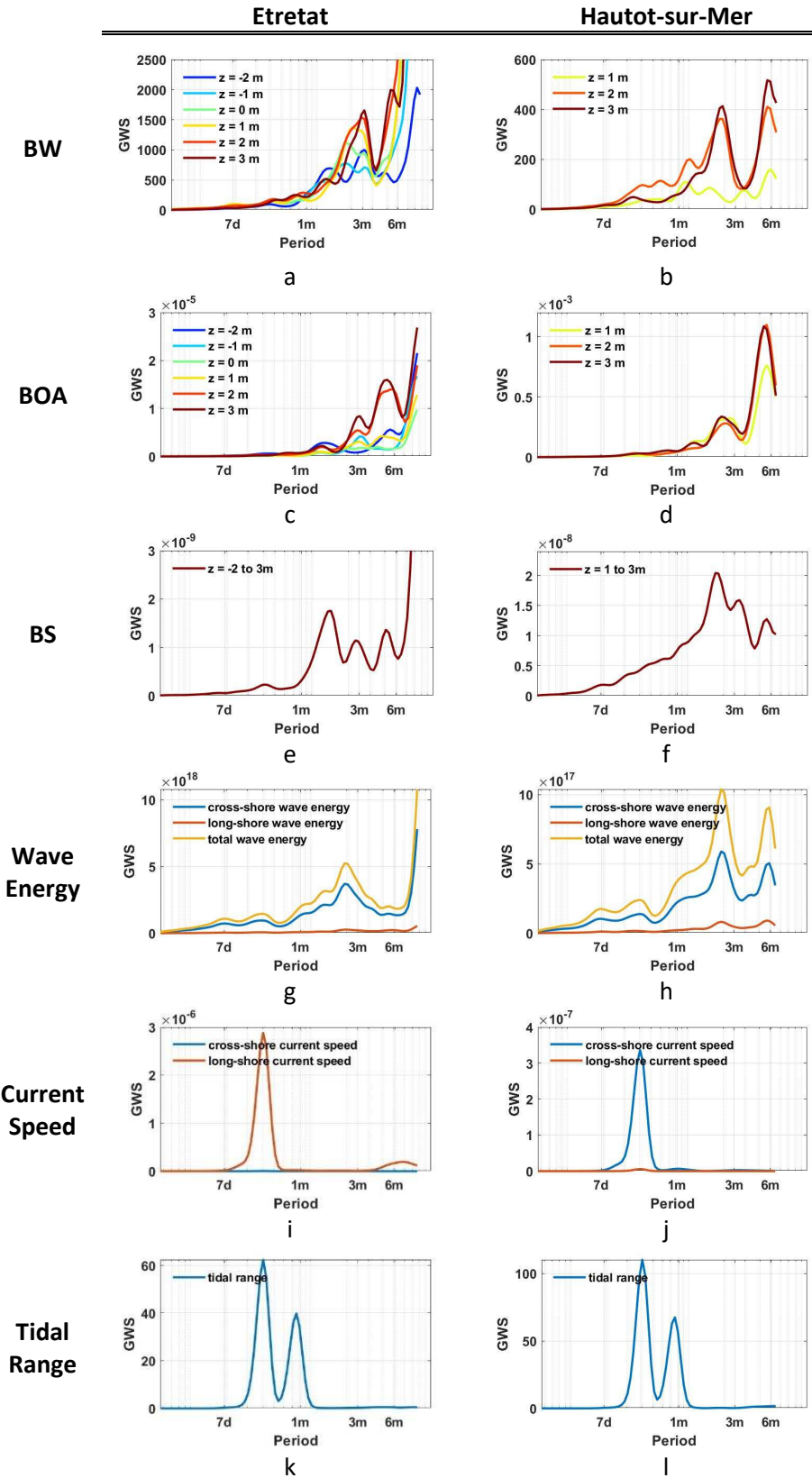


Figure 11 - Global Wavelet Spectrum (GWS) calculated from beach width (a, b), beach orientation angle (c, d), beach slope (e, f), wave energy (g, h), current speed (i, j) and tidal range (k, l) time series in Etretat (left) and Hautot-sur-Mer (right).

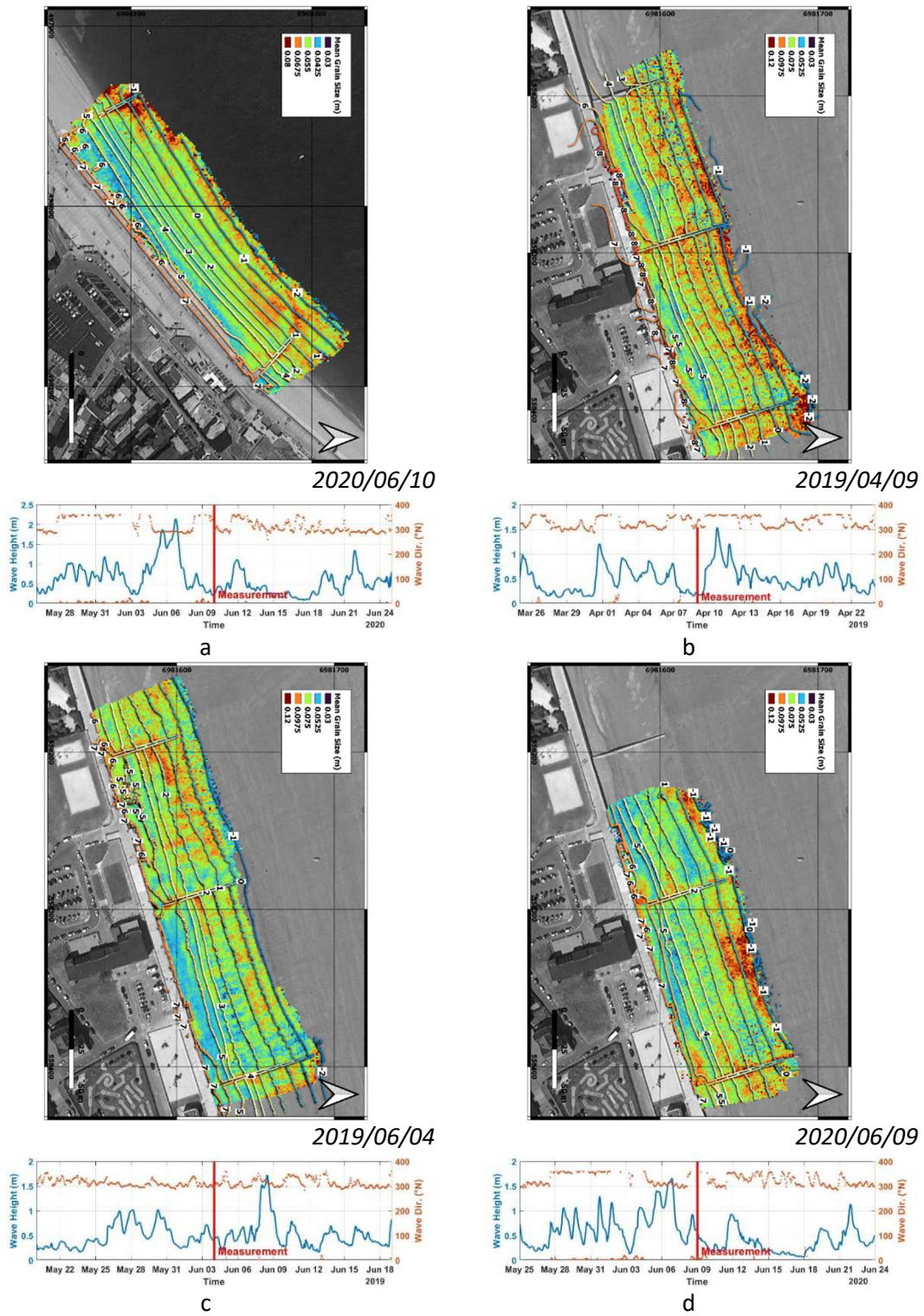


Figure 12 – Maps of mean clast length measured in Etretat on 2020/06/10 (a) and Hautot-sur-Mer on 2019/04/09 (b), 2019/06/04 (c) and 2020/06/09 (d). Contour lines of elevation are indicated for each round elevation with a vertical separation of 1 m. Hydrodynamic conditions are provided for a 30-day period centered on the UAV measurement campaign including the wave significant height (blue line, left y axis) and the wave direction (orange dots, right y axis).

Table 1 - Morphological characteristics of beaches at Etretat and Hautot-sur-Mer

Sites	Etretat	Hautot-sur-Mer
Average tidal range	6.08 m	6.79 m
Max tidal range	9.13 m	9.86 m
Min tidal range	3.20 m	2.96 m
Lowest Water Level (LWL) (datum: IGN69)	-4.80 m	-4.45 m
Beach Length	1000 m	1100 m
Beach width at LWL	150 m	210 m
Pebble ridge slope	> 12 %	> 10 %
Pebbles D50	60 mm	75 mm
Sand D50	0.80 mm	0.18 mm

Table 2 - Percentage of the total variability explained by the EOF components in Etretat and Hautot-sur-Mer

Site	Principal Components							Total
	1	2	3	4	5	6	7	
Etretat	62.4	14.1	5.8	3.9	2.3	2.0		90.5
Hautot-sur-Mer	46.1	14.8	7.0	4.3	3.4	3.2	2.4	81.2

Table 3 – Summary of the identified temporal periods of variability in morphological and hydrodynamical signals in Etretat and Hautot-sur-Mer

Periods (months)	≤1	2	3	4	5	6	7	≥8	
BW		X	X		X			X	Etretat
BOA		X	X		X			X	
BS		X	X		X			X	
WE		X						X	
CS	X								
TR	X								
BW		x				X			Hautot-sur-Mer
BOA		X				X			
BS		X	X			X			
WE		X				X			
CS	X								
TR	X								

Table 4 - Grain size results in meters for each UAV measurement campaign.

Site	Date	D16	D50	D84	Mean	Std
Etretat	2020/06/10	0.042	0.060	0.069	0.056	0.017
Hautot-	2019/04/09	0.056	0.074	0.108	0.082	0.029
sur-	2019/06/04	0.048	0.067	0.096	0.072	0.026
Mer	2020/06/09	0.051	0.069	0.098	0.075	0.028